The Astrophysical Journal, 943:111 (26pp), 2023 February 1 https://doi.org/10.3847/1538-4357/aca6e7
© 2023. The Author(s). Published by the American Astronomical Society.
OPEN ACCESS

Nonequilibrium Ionization Modeling of Petschek-type Shocks in Reconnecting Current Sheets in Solar Eruptions

Chengcai Shen, John C. Raymond, and Nicholas A. Murphy
Center for Astrophysics | Harvard & Smithsonian, 60 Garden Street Cambridge, MA 02138, USA; chengcaishen@cfa.harvard.edu
Received 2022 June 3; revised 2022 October 27; accepted 2022 October 27; published 2023 January 31

Abstract

Nonequilibrium ionization (NEI) is essentially required for astrophysical plasma diagnostics once the plasma status departs from the assumption of ionization equilibrium. In this work, we perform fast NEI calculations combined with magnetohydrodynamic (MHD) simulations and analyze the ionization properties of a Petschek-type magnetic reconnection current sheet during solar eruptions. Our simulation reveals Petschek-type slow-mode shocks in the classical Spitzer thermal conduction models and conduction flux-limitation situations. The results show that under-ionized features can be commonly found in shocked reconnection outflows and thermal halo regions outside the shocks. The departure from equilibrium ionization strongly depends on plasma density. In addition, this departure is sensitive to the observable target temperature: the high-temperature iron ions are strongly affected by the effects of NEI. The under-ionization also affects the synthetic SDO/AIA intensities, which indicates that the reconstructed hot reconnection current sheet structure may be significantly underestimated either for temperature or apparent width. We also perform an MHD-NEI analysis on the reconnection current sheet in the classical solar flare geometry. Finally, we show the potential reversal between the under-ionized and over-ionized states at the lower tip of reconnection current sheets where the downward outflow collides with closed magnetic loops, which can strongly affect multiple SDO/AIA band ratios along the reconnection current sheet.

Unified Astronomy Thesaurus concepts: Ionization (2068); Magnetohydrodynamical simulations (1966); Shocks (2086); Ultraviolet astronomy (1736)

Supporting material: animation

1. Introduction

Magnetic reconnection, or the breaking and rejoining of magnetic field lines in a highly conducting plasma, is commonly believed to be a fundamental process during solar eruptions, and it plays a key role in rapid magnetic energy release (e.g., Shibata & Magara 2011). It is commonly believed that reconnection involves rapid changes in temperature and density in reconnection regions of order 10^7 K in solar coronal environments. As an important observable signal of magnetic reconnection, such high-temperature reconnection current sheets have been frequently reported in the literature with different instruments: SOHO/UVCS (e.g., Ciaravella et al. 2002; Ko et al. 2003; Ciaravella & Raymond 2008), SDO/AIA (e.g., Savage et al. 2010; Reeves & Golub 2011; Cheng et al. 2018), Hinode/EIS (e.g., Warren et al. 2018; Imada 2021). Although the high-temperature reconnection outflow is predicted in both theoretical reconnection models and numerical experiments, the observable emission of the hot plasma (e.g., the emission from high ionization Fe lines) does not exactly reveal the temperature and density of the reconnection current sheet both in space and time due to the effects of nonequilibrium ionization (NEI; e.g., Shen et al. 2013b). It is worth mentioning that the observable reconnection current sheets are due to hot plasma material emissions in reconnection regions, which may differ from the theoretical current sheet in models. Therefore, we follow the term "current sheet" but refer to it as general dissipation and exhaust regions where the reconnection outflows and other relevant phenomena (e.g., slow-mode and fast-mode shocks) are expected in different plasma environments.

Around the reconnection current sheet, if the plasma is rapidly heated due to reconnection, then the ion charge states would correspond to lower temperatures than the actual temperature for a sizable duration longer than the dynamic timescale, and the plasma is referred to as under-ionized. If the plasma cools rapidly (e.g., due to adiabatic expansion), then the ionization states would correspond to higher than the actual temperature, and the plasma is over-ionized. In either case, if the plasma is in an NEI state, its ionization state must be obtained by considering time-dependent ionization. For instance, in a typical high-temperature solar flare environment with temperature $T \sim 10^7$ K, plasma density $n_e \sim 10^9\,\mathrm{cm}^{-3}$, magnetic field strength $B \sim 50$ G, and a characteristic length $L \sim 50$ Mm, the Alfvénic transit time is about 15 s, and the thermal conduction timescale is ~25 s. The above two typical dynamic timescales are generally much shorter than the ionization (and recombination) times ($\sim 10^3$ s) according to the characteristic equilibration density-weighted timescale, of order $10^{12}\,\mathrm{cm}^{-3}$ s, for Fe ions (Smith & Hughes 2010).

NEI effects have been reported in the post-coronal mass ejection (CME) plasma during solar eruptions in several models. Ko et al. (2010) modeled the UV and X-ray emission, including NEI states in a Petschek-type reconnection flow in the post-CME current sheet. They found that the predicted emission intensities are consistent with SOHO/UVCS and Hinode/X-ray observations. Shen et al. (2013b) performed a post-processed NEI analysis in a large-scale reconnection current sheet beneath the erupted CME in a magnetohydrodynamic (MHD) model. They calculated the time-dependent

Original content from this work may be used under the terms of the Creative Commons Attribution 4.0 licence. Any further distribution of this work must maintain attribution to the author(s) and the title of the work, journal citation and DOI.

ionization states using the numerical simulation data from Reeves et al. (2010), and predicted the UV/EUV emission intensity. It was found that ionization charge states can be significantly underestimated (or overestimated) by up to a factor of 2 compared with the assumption of equilibrium ionization (EI) along the current sheet. Recently, Lee et al. (2019) investigated the hot plasma sheet observed by SDO/AIA and Hinode/XRT on 2012 January 27. They calculated intensity ratios between different narrow-band images and compared them with the NEI modeling emission, and suggested that the ratio–ratio plot for intensities in different passbands can be used to express how far the plasma departs from EI. For the large solar flare on 2017 September 10 observed by Hinode/EIS, Imada (2021) reported that observed Fe XXIV/Fe XXIII ratios are consistent with the effects of time-dependent ionization at a constant electron temperature (~25 MK). This research also pointed out that NEI is required to investigate the temperature gradient in the magnetic reconnection region from density, temperature, and velocity diagnostics.

In general, the plasma inside the reconnection region is expected to be in an under-ionized state due to rapid heating processes that occur during reconnection. For example, Imada et al. (2011) analyzed the time-dependent ionization in steady Petschek-type reconnection models. They pointed out that iron ions are mostly in NEI states in the reconnection region, and line emissions are significantly different from those determined from the assumption of EI. However, an important question is still not well understood: how does NEI affect the fine structure of observable current sheets in various realistic magnetic reconnection regions? In recent decades, a set of reconnection models have been proposed, but which model drives solar eruptions is still an open question. Petschek-type reconnection (Petschek 1964; Forbes & Priest 1987) is an important mechanism in the solar atmosphere among different reconnection models, such as the classical Sweet–Parker current sheet (Parker 1957; Sweet 1958) and plasmoid instabilities that develop inside it (e.g., Loureiro et al. 2007; Bhattacharjee et al. 2009; Ni et al. 2010; Huang & Bhattacharjee 2016), and turbulent reconnection where the magnetic energy is supposed to be cascading in small-scale structures and heats the diffusion region (e.g., Lazarian & Vishniac 1999). Recently, Lin et al. (2021) pointed out that Petschek-type magnetic reconnection can be induced using a simple resistivity gradient in the reconnection outflow direction. The localized X-point is also predicted by Forbes et al. (2018) in the theoretical analysis of large-scale CME/flare eruptions. Therefore, studies of the Petschek-type reconnection and detailed emission features in NEI are important to investigate the plasma properties of the reconnection current sheet.

The high temperatures inside the reconnection current sheet can be produced by several processes, including ohmic heating in reconnection sites (generally referred to as X-points with the highest current), adiabatic compression, thermal conduction, slow-mode shocks along the two sides of the current sheet, and fast-mode shocks where super-magnetosonic reconnection outflows impact closed magnetic loop structures such as flare loops. In order to accurately simulate the ionization states and predict the corresponding emission of a reconnection current sheet, it is important to incorporate both the above physical processes and time-dependent ionization in a self-consistent model. In our previous models (Shen et al. 2013a, 2015, 2017), we employed post-processed methods to perform NEI calculations using MHD simulation results, especially temperature, density, and plasma flow evolution history. However, the post-processed NEI method depends on the trajectory of the streamline in which errors could be introduced due to the flow field interpolation in time (and space). It is also difficult to trace plasma evolution in turbulent flow regions, and it is not possible to self-consistently compute the radiative cooling rate during the MHD simulation. Therefore, an NEI calculation that can be incorporated into the MHD model itself is required for performing accurate NEI analysis in the reconnection current sheet. This kind of ionization solver has been reported in other astrophysical research regimes. Orlando et al. (2003) investigated the effects of NEI in the compact flare loop by combining the NEI calculation within the hydrodynamic (HD) modeling. An NEI solver (Zhang et al. 2018) using the eigenvalue method (e.g., Masai 1984; Hughes & Helfand 1985; Smith & Hughes 2010) and the AtomDB database (Foster et al. 2018) has been developed to perform fast NEI calculations in the FLASH code (Fryxell et al. 2000), and has been used to analyze the NEI in supernova remnants (e.g., Zhang et al. 2019). Charge states in the solar wind have been calculated using the plasma electron temperature, density, and velocity in several solar wind simulations such as the Michigan Ionization Code model (e.g., Landi et al. 2012; Landi & Lepri 2015) and Magnetohydrodynamic Algorithm outside a Sphere model (e.g., Lionello et al. 2019).

In this paper, we describe a model that combines the NEI calculation in MHD simulations in a public code: Athena (Stone et al. 2008). In Section 2, we briefly summarize the NEI solver in the Euler framework and the MHD modeling setup. In Section 3, we analyze the NEI properties around the Petschek-type reconnection current sheet, and predict EUV emissions. Then we discuss how the asymmetrical configuration of the reconnection current sheet affects the NEI properties. A discussion and conclusions are given in Sections 4 and 5.

2. Description of the Numerical Method

In this section, we describe how to include the NEI solver in a well-developed MHD code. In this paper, we focus on the application using the Athena code, but this process will be similar to other grid-based MHD codes. The governing resistive MHD equations in our combined MHD-NEI simulations are the following:

$$\frac{\partial \rho}{\partial t} + \nabla \cdot (\rho \boldsymbol{v}) = 0, \tag{1}$$

$$\frac{\partial \rho \boldsymbol{v}}{\partial t} + \nabla \cdot (\rho \boldsymbol{v}\boldsymbol{v} - \boldsymbol{B}\boldsymbol{B} + \boldsymbol{P}^*) = 0, \tag{2}$$

$$\frac{\partial \boldsymbol{B}}{\partial t} - \nabla \times (\boldsymbol{v} \times \boldsymbol{B}) = \eta_m \nabla^2 \boldsymbol{B}, \tag{3}$$

$$\frac{\partial E}{\partial t} + \nabla \cdot [(E + P^*)\boldsymbol{v} - \boldsymbol{B}(\boldsymbol{B} \cdot \boldsymbol{v})] = S, \tag{4}$$

where $\boldsymbol{P}^*$ is a diagonal tensor with components $\boldsymbol{P}^* = P + B^2/2$ (with P the gas pressure), and $E = \frac{P}{\gamma - 1} + \frac{1}{2}\rho v^2 + \frac{B^2}{2}$ is the total energy density, $\gamma = 5/3$ is the adiabatic index, and the energy source term $S = \mu_0 \eta_m j^2 + \nabla_{\parallel} \cdot \kappa \nabla_{\parallel} T$, which includes ohmic dissipation and thermal conduction. The quantities ρ, $\boldsymbol{v}$, $\boldsymbol{B}$, and T are mass density, flow velocity, magnetic field, and temperature, respectively. Here, μ_0, η_m, and κ are the magnetic

permeability of free space, magnetic diffusivity, and the parallel component of the Spitzer thermal conduction tensor.

The time-dependent ionization equations in an Eulerian framework can be described as follows:

$$\frac{\partial f_i}{\partial t} + \nabla \cdot f_i \boldsymbol{v} = n_e \times [C_{i-1} f_{i-1} - (C_i + R_i) f_i + R_{i+1} f_{i+1}], \quad (5)$$

where f_i is the ion fraction of the ith ionization state, C_i and R_i are ionization and recombination rate coefficients for these ions. n_e is the electron density, which is $\sim$1.2 proton density for fully ionized plasma in our single-fluid MHD model. For an element with the atomic number Z, f_i covers all $Z+1$ ion charge states. Here, the C_i and R_i rates are functions of temperature, which are computed from the MHD simulations at each time step. In optically thin plasma, such as solar corona, the most important ionization/recombination processes are collisional ionization, excitation-autoionization, radiative recombination, and dielectronic recombination. Therefore, we consider the above electron temperature (and density) dependent ionization and recombination rates in our models. Because the right-hand side of Equation (5) does not explicitly involve the time (and spatial) operations, we apply the operator splitting method and set it as an NEI source term. In this way, Equation (5) can be separately solved in two steps: the advection part $\left(\frac{\partial f_i}{\partial t} + \nabla \cdot f_i \boldsymbol{v} = 0\right)$, and the source part $\left(\frac{\partial f_i}{\partial t} = n_e[C_{i-1} f_{i-1} - (C_i + R_i) f_i + R_{i+1} f_{i+1}]\right)$. For the advection part, it is easy to apply a similar scheme in the MHD code itself. In fact, it is even more convenient to solve the advection part through the passive scalars in the MHD mass equation (Equation (1)), which is usually introduced in most MHD codes. In the Athena code, the mass equation with passive scalars is

$$\frac{\partial (s_i \rho)}{\partial t} + \nabla \cdot (s_i \rho \boldsymbol{v}) = 0, \quad (6)$$

where $s_i (i = 1, \ldots, N)$ are the mass fractions of N passive scalars. The ion fraction for a single particular element with $N+1$ charge states can be directly obtained as $f_i = s_i / \sum s_i$.

2.1. Eigenvalue Method

We solve the source part of the time-dependent ionization equations using the eigenvalue method (e.g., Hughes & Helfand 1985; Smith & Hughes 2010; Shen et al. 2015), in which ionization equations can be represented in matrix form, and the exact exponential solution can be calculated using matrix multiplication. The time-dependent ionization equation can then be written as

$$\frac{\partial \boldsymbol{F}}{\partial t} = n_e \boldsymbol{A} \cdot \boldsymbol{F}, \quad (7)$$

where $\boldsymbol{F}$ is a vector containing ion fractions f_i, and $\boldsymbol{A}$ is the matrix containing ionization and recombination rate coefficients (C_i and R_i) on the right-hand side of Equation (5). Using the eigenvalues and eigenvectors of the matrix $\boldsymbol{A}$, the solution of Equation (7) can be presented in the form

$$\frac{\partial \boldsymbol{F}'}{\partial t} = n_e \lambda \cdot \boldsymbol{F}', \quad (8)$$

where λ is a diagonal matrix containing eigenvalues of the matrix $\boldsymbol{A}$. By defining $\boldsymbol{V}$ as the matrix of eigenvectors of $\boldsymbol{A}$ with all eigenvalues, $\boldsymbol{F}'$ can then be defined as $\boldsymbol{V}^{-1} \cdot \boldsymbol{F}$. For a particular temperature (T_c), it is easy to get corresponding eigenvalues and eigenvectors. The solution of Equation (8) can be reduced to simple exponentiation: $\boldsymbol{F}' = \boldsymbol{F_0} \exp(-n_e \lambda(T_c) t)$. Here, $\boldsymbol{F}_0$ is the initial condition containing ion fractions for this element. Hence, the ion fraction vector $\boldsymbol{F}$ for the ionization state at any time is easy to compute by the matrix multiplication using $\boldsymbol{F}'$ and the eigenvector matrix at temperature T_c. This method is very robust and has an advantage over explicit methods that take a very long time step at a single temperature that would result in an EI state. Once we precalculated eigenvalues and eigenvectors for all ions on a temperature grid, the code can reload eigenvalues and eigenvectors, and quickly perform the above calculation.

We follow this eigenvalue method and apply our well-tested NEI code (Shen et al. 2015) in the following combined MHD-NEI simulations. This NEI code[1] was originally developed using Fortran and has been restructured into a C module that can efficiently perform the in-line NEI calculation in Athena. We also use updated atomic data from the CHIANTI database (version 9, Dere et al. 2019) to create lookup tables, including all necessary ionization and recombination rates, and eigenvalue corresponding matrices. We employ this method in several test projects, such as one-dimensional shock tubes, and compare the results with the post-processed NEI calculations (see Appendix A for details). The result shows that this in-line NEI module calculates charge states accurately, and it can be used in complex problems such as shocks.

2.2. MHD Model Setup

We set up two types of MHD models to study reconnection outflows: (i) steady Petschek-type reconnection, and (ii) realistic reconnection current sheet during solar flares. In model (i), the initial condition consists of a preexisting Harris-type current sheet along the y-direction with the nondimensional width $w = 0.025$ as follows:

$$B_x(x, y) = 0, \quad (9)$$

$$B_y(x, y) = \tanh\left(\frac{x}{w}\right), \quad (10)$$

$$B_z(x, y) = (1 - B_y(x, y)^2)^{1/2}, \quad (11)$$

$$p(x, y) = \beta_0 / 2, \quad (12)$$

$$\rho(x, y) = 1. \quad (13)$$

Here, β_0 is the background plasma β (the ratio of the magnetic pressure to gas pressure) in the ambient region. The initial current sheet is then in dynamical equilibrium with uniform temperature and density. In order to have the system evolve rapidly from the initial steady state to a fast reconnection phase, we introduce a perturbation magnetic field B_{1x} and B_{1y} on this

[1] NEI code: https://github.com/ionizationcalc/time_dependent_fortran.

preexisting current sheet as follows:

$$B_{1x}(x, y) = \frac{2\pi}{L_y} A_{\rm pert} \cos\left(\frac{\pi x}{L_x}\right) \sin\left(\frac{2\pi(y - y_c)}{L_y}\right) B_0, \quad (14)$$

$$B_{1y}(x, y) = -\frac{2\pi}{L_x} A_{\rm pert} \sin\left(\frac{\pi x}{L_x}\right) \cos\left(\frac{2\pi(y - y_c)}{L_y}\right) B_0. \quad (15)$$

Here, $A_{\rm pert} = 0.0001$ is the nondimensional perturbation strength located at $[x = 0.0,\ y_c = 0.0]$. L_x and L_y are nondimensional perturbation wavelengths that are set to 2 and 2 in order to minimize perturbations at boundaries. We set the symmetrical boundary condition along the center of the system ($x = 0$) and the open boundary condition at other sides. The simulation domain then covers the right half of the reconnection region, ranging from $x = 0$ to 1 and $y = -1$ to 1. To drive Petschek-type reconnection, we introduce an anomalous strong diffusion at the system center with a double-Gaussian distribution in space where the equivalent magnetic Reynolds number is about 10^4. Driven by the initial perturbation on magnetic fields and the localized enhanced diffusion at the system center, the initial current sheet gradually develops into the single X-point reconnection geometry associating with a pair of slow-mode shocks extended along current sheet edges.

Our second type of reconnection model is based on the classical two-ribbon flare configuration, where the magnetic reconnection is expected to appear in a vertically extended current sheet above the reconnected post-flare loops, which is also referred to as the classical CSHKP model (Carmichael 1964; Sturrock 1968; Hirayama 1974; Kopp & Pneuman 1976). Following our previous modeling setups (e.g., Shen et al. 2011, 2018), we also start the simulation from a thermal and dynamical equilibrium current sheet structure but include the line-tied boundary condition at the lower side to represent the solar surface where the magnetic field is rooted into the boundary and the plasma cannot slip. To simulate Petschek-type shocks, we also apply a locally enhanced resistivity as in the above discussion.

2.3. Thermal Conduction

Thermal conduction can significantly affect plasma properties during magnetic reconnection. In numerical simulations, one of the direct impacts is that the conduction along magnetic field lines may cause wider reconnection outflows (Yokoyama & Shibata 1997). A high-temperature plasma region (also referred to as thermal halo) has been proposed in both analytical and numerical models (e.g., Yokoyama & Shibata 2001; Seaton & Forbes 2009). However, the thermal conductive flux could be overestimated in the shock front where the temperature jump is extremely sharp and the corresponding conductive flux based on the Spitzer coefficients becomes nonphysical. There is also a potential jump at a collisionless shock that inhibits electron transport from downstream to upstream. In general, the conductive flux along the magnetic field lines is given by $-\nabla_\parallel \cdot \kappa \nabla_\parallel T$, where the Spitzer conductivity κ for elections is the nonlinear function of plasma temperature in the form of

$$\kappa = 10^{-6} T^{5/2}\ {\rm erg\ K^{-1}\ cm^{-1}\ s^{-1}}. \quad (16)$$

The above classical coefficient is valid under the assumption that the mean free path ($L_{\rm mfp}$) of electrons is much shorter than the temperature scale length ($L_T = T/|\nabla T|$). For extremely sharp temperature changes, such as a shock front, the mean free path becomes comparable to or larger than the temperature scale length. Furthermore, nonthermal particles are expected to be accelerated in shocks, so accurately resolving the conductive flux requires detailed information on particle velocity distributions around the shock fronts. Instead of discussing the thermal conductive flux in various non-Maxwellian particle velocity distributions, we focus on the ionization behavior inside the high-temperature reconnection current sheet in this work. Therefore, we introduce an additional conductive flux limitation on the classical Spitzer flux form to limit the nonphysical thermal conduction around the shock front. We set the upper limit of conductive flux to be the saturation flux (e.g., Cowie & McKee 1977) when the electron mean free path is sufficiently large ($L_{\rm mfp} > L_T$). Following the method reported by Winter et al. (2011) in one-dimensional HD models, we also introduce a power-law factor in the Spitzer conductive flux when the mean free path is close to the temperature scale length (Rosner et al. 1986):

$$F_{\rm cond} \sim 0.11 \frac{L_{\rm mfp}^{-0.36}}{L_T} F_{\rm Spitzer}, \quad (17)$$

where $F_{\rm Spitzer}$ is the Spitzer conductive flux and $F_{\rm cond}$ is the modified flux. This approach allows us to obtain more realistic temperature distributions inside the reconnection current sheet, which is crucial for the NEI analysis. However, the conduction may depart more from the above Equation (17) due to the microinstabilities in the above flux-limitation models (Rosner et al. 1986), which is beyond the scope of this paper, and will be investigated in future work. For comparison, we also run the same model but with the classical Spitzer thermal conduction, which gives insight into how the thermal halo can develop in such an extremely strong thermal conduction situation. Therefore, the conductive flux-limited simulation can be thought of as the lower limit of the effects of conduction, while the classical Spitzer heating flux model is close to the upper limit of the thermal conduction modeling.

3. Results

The primary simulation parameters for different cases are listed in Table 1. Figure 1 shows the Petschek-type magnetic reconnection configuration in our simulations. After the initial perturbation and the early slow magnetic diffusion process, the reconnection process is close to the steady phase at the time $t \sim 6t_0$ (for example, $\sim$520 s in Case A2 with the chosen characteristic time $t_0 = 87$ s), when the reconnection inflow and outflow speeds do not significantly change. The reconnection X-point is located at the origin ($x = 0,\ y = 0$) due to the localized magnetic resistivity at this position. From the X-point to two sides of the current sheet, a pair of slow-mode shocks can be clearly identified where the magnetic field dramatically changes and the plasma is abruptly heated to more than $\sim 10^7$ K. These shock fronts also can be seen from plasma profiles crossing the edge of the current sheet, and the shock jump conditions are met with the finite shock thickness in $2 \sim 3$

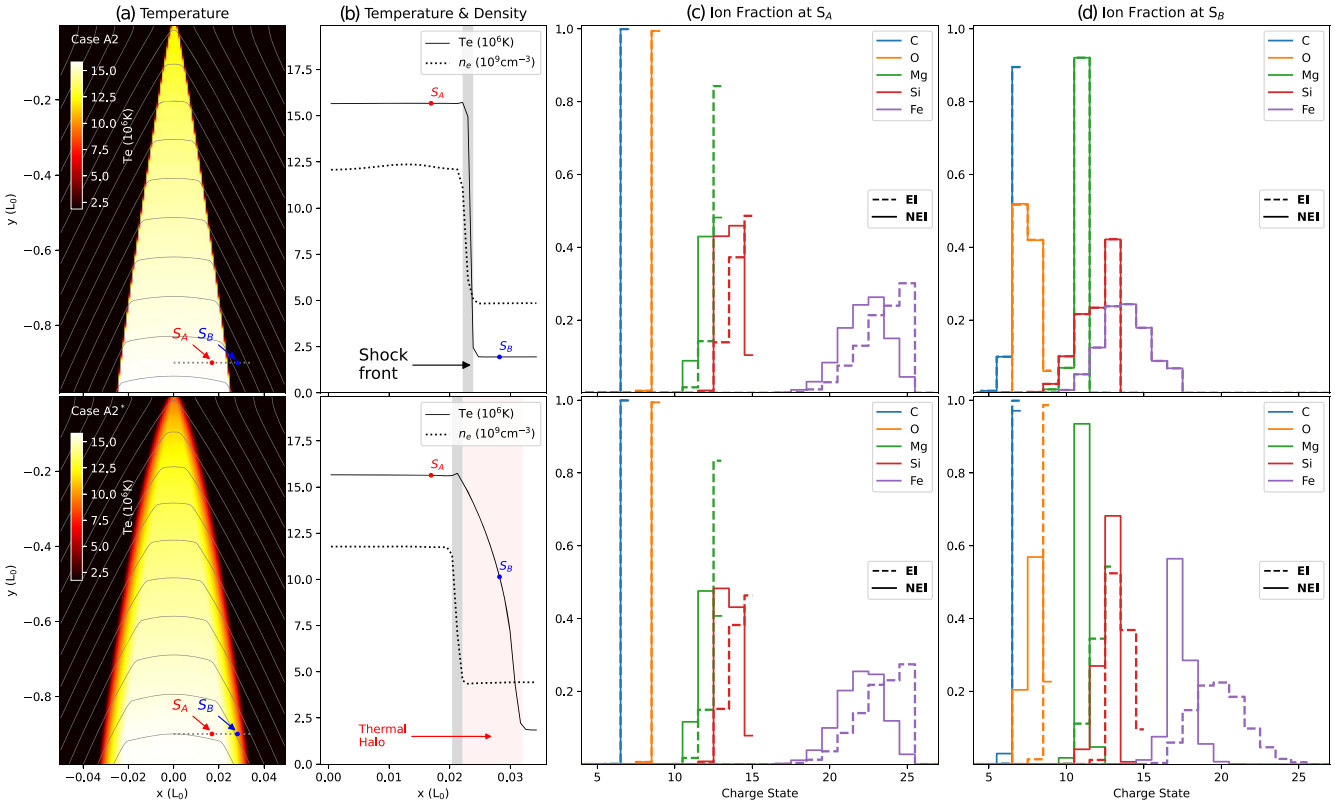

Figure 1. Temperature and density distribution across the Petschek-type shocks in Cases A2 and A2*. Here, Case A2 employed the conductive flux limitation and Case A2* is for the classical Spitzer conduction simulation. Two sampling points (S_A, S_B) have been chosen along the dotted horizontal sampling line at $y = -0.9L_0$. Here, the nondimensional characteristic length $L_0 = 1.5 \times 10^8$ m. Panel (b) shows the temperature and density profiles along the sampling line shown in (a). The gray- and red-shaded regions indicate the shock front and thermal halo regions, respectively. Panels (c) and (d) show the ion fractions of C, O, Mg, Si, and Fe at S_A and S_B. The solid lines denote the NEI results, and the dashed lines represent the EI. The charge state in the horizontal axis is in spectroscopic notation in which Fe XII means Fe $^{11+}$.

Table 1
Primary Simulation Parameters for Different Cases

	Density		
Plasma β	5×10^9 cm^{-3}	1×10^9 cm^{-3}	5×10^8 cm^{-3}
0.04	Case A1	Cases B1, D	Case C1
0.05	Cases A2, A2*	Case B2	Case C2
0.075	Case A3	Case B3	Case C3
0.1	Case A4	Case B4	Case C4

Note. Case A2* used the Spitzer conduction coefficient. Case D includes gravity in the y-direction with plasma $\beta = 0.04$ and density $n_e = 1.0 \times 10^9$ cm^{-3} at $y = 1.0L_0$.

MHD simulation grid cells (see more details in Appendix B and Figure 16). At this time, the reconnection inflow speed ($\sim V_x$) is about 100 km s^{-1} while the outflow velocity (V_y) can reach the Alfvén speed of >1000 km s^{-1}. This configuration, therefore, shows a quick reconnection process with the nondimensional reconnection rate $M_A \sim 0.1$ ($M_A \equiv V_{\rm inflow}/V_{\rm outflow}$).

As shown in Table 1, we ran a set of combined MHD-NEI simulations for different densities and temperatures. We chose typical solar active region parameters, with the initial background temperature of 2×10^6 K in all cases. The temperature inside the reconnection current sheet then depends on β, and can be estimated according to the shock jump condition:

$$\frac{T_{\rm Dn}}{T_{\rm Up}} = 1 + \frac{2}{5\beta}. \quad (18)$$

Here, $T_{\rm Dn}$ is the downstream (or shocked plasma) temperature inside the reconnection current sheet, and $T_{\rm Up}$ is the upstream (or the background coronal) temperature. We change the plasma β from 0.04, 0.05, 0.075 to 0.1 to obtain post-shock temperatures 2.2×10^7, 1.8×10^7, 1.267×10^7, and 10^7 K, respectively. Due to the magnetic energy dissipation and the reduction of the ambient field during the evolution of the system, the post-shock temperatures measured in the following sections decline slightly to around 1.8×10^7, 1.6×10^7, 10^7, 8×10^6 K until the system evolves into a phase with relatively steady reconnection. The plasma density can be expected to increase a factor of $2.36 \sim 2.2$ in shocked regions for the above β list, according to the formula $\rho_{\rm Dn}/\rho_{\rm Up} = 5(1+\beta)/(2+5\beta)$ (e.g., in Ko et al. 2010). Because the ionization (or recombination) timescale is proportional to the plasma density, models with low density are expected to cause stronger effects of NEI. We then set the ambient density to 5×10^9 cm^{-3} in the Case A series for the typical coronal environment, but also run the more tenuous density of 10^9 cm^{-3} and 5×10^8 cm^{-3} in the Case B series and Case C series for comparison.

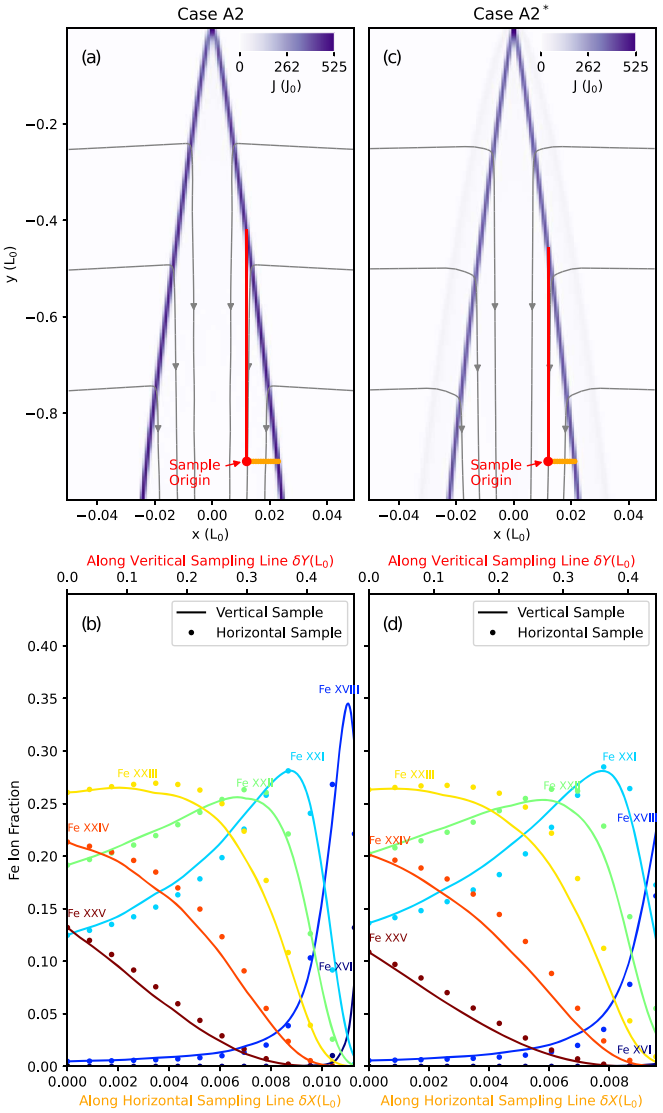

Figure 2. Iron ion fraction distribution across the Petschek-type shocks in Cases A2 and A2*. In the top panels, the gray streamline shows the plasma flows. The strong current density (J) indicates the position of shock fronts. In panels (b) and (d), ion fraction distributions inside reconnection current sheets are shown along the two chosen sampling lines in the vertical and horizontal directions.

3.1. Under-ionized Plasma

In this section, we analyze the ionic charge state in the Petschek-type reconnection current sheet and surrounding regions, and show how the ionization state departs from EI. We first compare Case A2 and Case A2* with the conduction flux limit simulation and classical Spitzer conduction coefficients, respectively. Magnetic configurations are similar among the two cases, as shown in Figure 1(a). In the downstream region (or inside the current sheet), the plasma is heated to $\sim$15.7 MK from the background coronal temperature of $\sim$1.95 and $\sim$1.85 MK for Cases A2 and A2*, respectively. The plasma density jumps from $\sim 5 \times 10^9$ to 1.2×10^{10} cm^{-3} crossing the shock front (Figure 1(b)). Outside the current sheet (or in the upstream region of the shocks), a temperature *halo* region (red shading in Figure 1(b) is clear in Case A2* due to the strong thermal conduction. On the other hand, once the thermal conduction flux limitation is employed in Case A2, the thickness of the thermal halo decreases to the grid size. Case A2 also appears to have a slightly higher temperature/density compared with Case A2* inside the reconnecting current sheet due to the reduced thermal conduction.

We then investigate the charge state distribution at two typical sampling points (S_A and S_B) in the shock downstream (inside reconnection current sheet) and upstream (in ambient regions), respectively. Figures 1(c) and (d) show the ion populations for chosen abundant elements in the solar corona, including C, O, Mg, Si, and Fe. Here, the solid lines indicate the time-dependent ionization results solved by the in-line NEI module, and the dashed lines indicate the EI, which depends only on the local temperature. At the point S_A, because the plasma is suddenly heated by the shock, ion populations of high charge states (e.g., Fe XXIV, Fe XXV) are clearly lower than the EI. The departure of NEI ion fractions from EI can be found in the ionization distribution profiles, where the solid lines (for NEI) are skewed toward lower charge states compared to the EI results (dashed lines). This result indicates that the plasma is clearly under-ionized. In the ambient region (S_B) beyond the thermal halo, on the other hand, the profiles are the same between the NEI and EI in Case A2 due to the unchanged plasma temperature and density. In the thermal halo region for Case A2*, the NEI profile at S_B also appears as under-ionized features because this plasma is preheated from the ambient corona temperature before it reaches the shock front.

The two-dimensional spatial distributions of ion fractions inside the Petschek-type reconnection current sheet are shown in Figure 2. In this figure, the high current density indicates the edges of the shock front in Figures 2(a) and (c) and the gray lines with arrows indicate the streamlines of the velocity fields in the MHD simulations for Case A2 and Case A2*. It is clear that the bulk plasma inflow toward the shock front is roughly along the horizontal direction (x-direction) outside the current sheet, and then rapidly turns to the reconnection outflow direction (y-direction) as it flows through the shock front. This behavior follows the Petschek reconnection theoretical expectation. In an ideal Petschek reconnection current sheet, the post-shock density, temperature, and velocity are uniform in both the x- and y-directions; the ionic distribution in the x-direction, therefore, entirely depends on the flow paths in the y-direction as shown by the solid red and orange color sampling lines in Figures 2(a) and (c). In other words, the ion's distribution along the red and orange sampling lines would be exactly the same in ideal situations. We then compare the chosen Fe ion fraction along the above two sampling lines starting from a random origin point, and ending on the shock front (Figure 2(b), (d)). The overall feature is that these two distributions (the dotted lines and solid lines) basically match each other. The distances of a sampling origin point away from the shock fronts can be determined by the Petschek shock angle as

$$\Delta_y = \frac{\Delta_x}{\tan(\theta)}. \tag{19}$$

Here, Δ_y and Δ_x are the distances to the shock front in the y- and x-directions, and θ is the shock angle in the downstream (also see the intersection angle between the y-axis and the shock edges in Figure 2).

In general, the plasma conditions are not uniform inside the current sheet in realistic models due to compression, which causes a slightly higher temperature away from the X-point

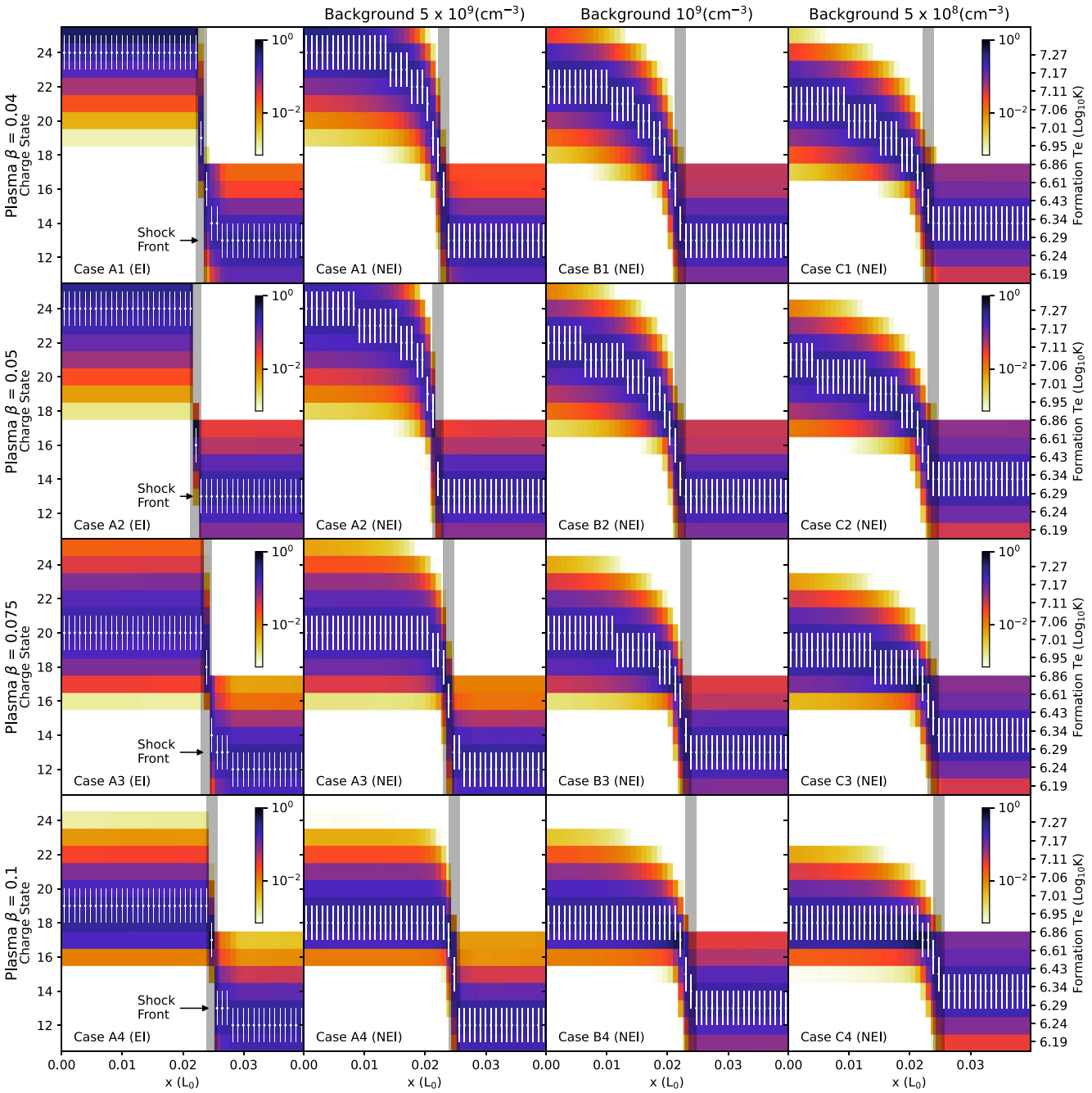

Figure 3. Fe ion fractions along the sampling line ($y = -0.9L_0$, the same as in Figure 1(a)) but in different cases. The left panel shows the EI results of the Case A series, and the right three panels represent NEI situations with different background coronal densities of 5×10^9, 10^9, and 5×10^8 cm^{-3}, respectively. From top to bottom, each row represents the different plasma β, 0.04, 0.05, 0.075, and 0.1, which are relative to the post-shocked plasma temperatures around 18, 16, 10, and 8 MK. The white vertical bars indicate the most dominant top three ions along the sampling line at each position. The right axis labels the corresponding formation temperature of each ion assuming EI.

(Figure 1). The velocity streamlines also tend to bend toward the system center (y-axis) as shown in Figures 2(a) and (c). Thus, parts of the sampling points along the horizontal orange sampling line show larger fractions on high ionic states compared with the vertical sampling line. This suggests that 2D distributions of ion populations inside the current sheet could be approximated by analyzing the plasma evolution along the y-directions in Petschek-type reconnection configurations (e.g., Lee et al. 2019). However, combined MHD-NEI modeling is essentially required to obtain accurate ion distributions.

3.2. Ionization Properties versus Temperature and Density

To investigate how plasma temperature and density impact the ion fraction distribution across the shock front, we compare the NEI features in detail for different simulation cases. In Figure 3, we show the ion population of dominant Fe ions along the horizontal sampling line (dotted lines at $y = -0.9L_0$ in Figure 1). The white vertical bars indicate the dominant three charge states at each location along this sampling line, and the background colors are for ion fractions. In the EI, as shown in the left panels in Figure 3, the Fe ion fractions are dominated

by the local temperature distribution, which is roughly uniform along the sampling line inside the reconnection current sheet due to thermal conduction. Therefore, the EI ion population of each Fe charge state would be the same along the x-direction. For example, the dominant three Fe ions are shown by dark purple colors in the top row in Figure 3 where the shock temperature is higher, $\sim 1.8 \times 10^7$ K, inside the current sheet. Outside the current sheet, the coronal temperature is about 2 MK and the corresponding main ion charge states are Fe XII $\sim$ Fe XIV along the sampling line, except near the shock fronts, where the background plasma may be slightly heated by compression in different plasma β environments during the magnetic reconnection process.

The right panels of Figure 3 show the NEI ion fraction along the sampling line when the reconnecting current sheet evolves to a steady phase and the density in the downstream side jumps to roughly 1.1×10^{10}, 2.3×10^9, 1.3×10^9 cm^{-3} for Cases A1, B1, and C1, respectively. Because the ionization timescale is inversely proportional to the electron density, the tenuous density is expected to cause more NEI effects. As shown in the first row of Figure 3, the dominant Fe ion quickly changes from Fe XIII to Fe XXIV in the high-density Case A1 in the post-shock region. In the low-density Case C1, the dominant Fe ion changes more slowly and finally approaches Fe XXI, which causes broader distributions of relatively low charge states (e.g., Fe XIV $\sim$ Fe XX) in the reconnection current sheet compared with the high-density case.

Another feature is that the effect of the NEI is not only sensitive to the electron density, but also substantially depends on the target temperature: the hot and tenuous plasma shows strong NEI features inside the current sheet compared with relatively dense and cooler plasma. The higher charge states generally will tend to show significant departures from EI. For example, the dominant ion is Fe XVIII when the temperature is about 8 MK as shown in the fourth row (Cases A4, B4, and C4). Though the ion fraction changes much more slowly in the low-density Case C4 and the higher charge states (e.g., Fe XX $\sim$ Fe XXV) show clear differences from the EI, the lower charge states (Fe XVII $\sim$ Fe XIX) are closer to the EI except in a narrow region near the shock front because the ionization rates of Fe ions increase more dramatically as the temperature increases, while the recombination rates change relatively slowly. The imbalance between the ionization and recombination processes becomes stronger in the higher-temperature cases. The under-ionized nature also causes the temperature of the reconnection current sheet that is usually derived under the assumption of EI to be lower than its actual temperature. For instance, the reconnection current sheet with dominant emission from Fe XXII would be thought to be $\log T = 7.11$ K under the assumption of EI. However, the *actual* plasma temperature can be higher than $\log T = 7.25$ K, as shown in Figure 3.

To compare the results of the assumption of NEI with the assumption of EI, we define the relative difference in ion populations between the assumption of NEI and EI as $f_{\rm diff} = (f_{\rm nei} - f_{\rm ei})/(f_{\rm nei} + f_{\rm ei})$, and plot out $f_{\rm diff}$ maps for each case in Figure 4. Here, f is for ion fractions, nei stands for NEI, and ei stands for EI. $f_{\rm diff}$ is a compressed scale to show departures in two directions, which gives $+1$ when the equilibrium ion fraction is close to zero and the nonequilibrium ion fraction is close to 1, and vice versa for $f_{\rm diff} = -1$. The relative value of the populations can then be obtained by

$$\frac{f_{\rm nei}}{f_{\rm ei}} = \frac{(1 + f_{\rm diff})}{(1 - f_{\rm diff})}. \tag{20}$$

For instance, $f_{\rm diff} = 0.25$ means that $f_{\rm nei} \sim 1.67 f_{\rm ei}$ and $f_{\rm diff} = 0.5$ correspond to $f_{\rm nei} \sim 3 f_{\rm ei}$, respectively.

The format of Figure 4 is similar to that of Figure 3, and the color maps range from -1 to 1 accordingly. The black contour lines denote the position where the NEI population is equal to the assumption of EI with $f_{\rm diff} = 0$, and the contours of $f_{\rm diff} = -25\%$, -50% are marked by dark red and red lines, respectively. Due to the under-ionized nature inside the current sheet, the high charge state ions (above the red lines in Figure 4) lie in the blue region that indicates that the fractions in the NEI are much smaller than in the EI, while the low charge state ions are red because the factions in the NEI are larger than in the EI. For dense plasma situations (e.g., Cases A1–A4 in Figure 4), the fraction of high charge states obviously departs from EI, especially in the local downstream region near the shock front. Even in the high-temperature and high-density environments (Case A1), the relative difference ($f_{\rm diff}$) in Fe XXV can be as high as 50% in a relatively wide region ($\sim 1.2 \times 10^6$ m from $x = 0.015 L_0$ to $x = 0.023 L_0$, with $L_0 = 1.5 \times 10^8$ m). If the background density is lower, $\sim 5 \times 10^8$ cm^{-3} (Cases C1–C4), all high charge state ions clearly depart from the assumption of EI.

On the other hand, the relative differences in $f_{\rm diff}$ are much smaller around the EI position (black lines) in low-temperature ranges. For instance, in Case A4, the EI ions are dominated by Fe XIX while ions ranging from Fe XIV to Fe XXIII are close to the EI states, with the $f_{\rm diff} < \sim 25\%$. This suggests that the shocked plasma can be close to the EI states for lower temperature current sheets (e.g., 8 MK) even if the density is lower than $\sim 5 \times 10^8$ cm^{-3}. In this case, the ionic fraction of lower ionization ions, such as Fe XIV and Fe XVIII, can be estimated based on the EI results. However, the reconnection current sheet of higher temperature (e.g., 18 MK and above) with low densities should be considered as in the NEI states. Inside such a current sheet, the population of most observable ions (e.g., Fe XVIII to Fe XXIV) may significantly depart from the assumption of EI up to about a factor of 3.

3.3. Shock Fronts in the Synthetic EUV Images

The high-temperature plasma sheets observed by EUV imaging instruments (e.g., SDO/AIA) above the post-flare loops are commonly thought of as the appearance of reconnecting current sheets. Some bright current sheet features observed in the SDO/AIA 94 Å and AIA 131 Å bands show a very similar morphology compared with theoretically predicted reconnecting current sheet structures. However, systematic analysis of how the NEI affects these EUV imaging observations is still rare. In particular, the EUV emission around Petschek-type shock fronts with NEI effects has not been fully understood in previous theoretical modeling studies. Therefore, we calculate the emission intensities using the NEI modeling results and obtain synthetic SDO/AIA images around Petschek-type shocks. Here, we include 14 elements that contribute significantly to coronal emission in the combined MHD-NEI simulations, including H, He, C, N, O, Ne, Mg, Al, Si, S, Ar, Ca, Fe, and Ni. For each element, the emission intensities are calculated using the NEI ionic population and the emissivity data from the atomic database, CHIANTI (Dere et al. 2019). For each ion of a chosen element, the line emission can be

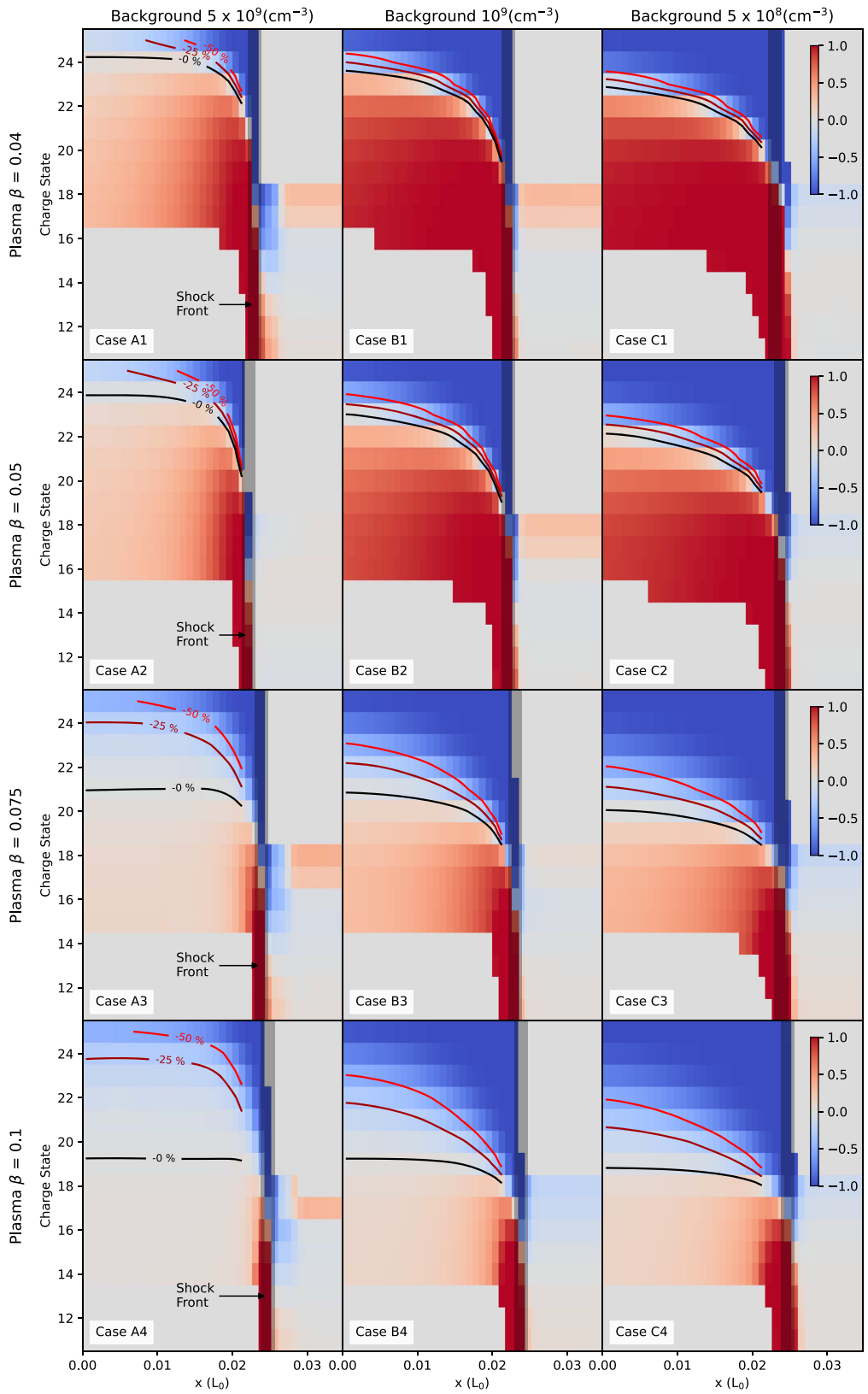

Figure 4. The relative difference in the Fe ion population between the NEI and EI, defined by $f_{\rm diff} = (f_{\rm nei} - f_{\rm ei})/(f_{\rm nei} + f_{\rm ei})$. The colored solid lines mark the position with $f_{\rm diff} = 0\%$, -25, and -50%.

calculated by

$$I_{\rm line}(\lambda) = \frac{n_x}{4\pi n_{\rm H}} \int G(T)\, d{\rm EM}(T), \qquad (21)$$

where $I_{\rm line}$ is in units of photons per cubic centimeter per second per steradian[1], λ is the wavelength, and $n_x/n_{\rm H}$ is the elemental abundance (Schmelz et al. 2012). $G(T)$ is the

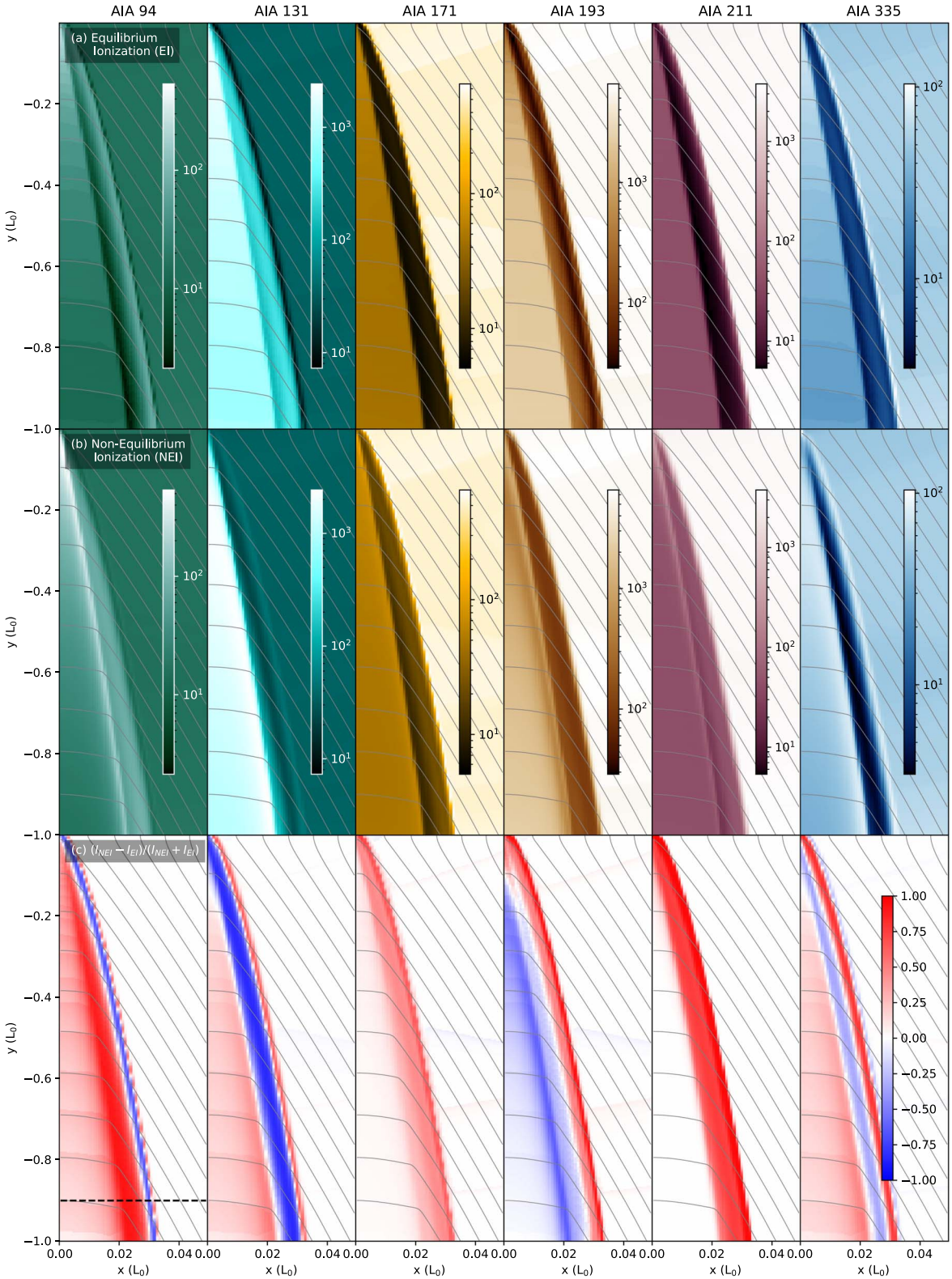

Figure 5. Synthetic SDO/AIA images for Case A2* with the classical Spitzer thermal conduction coefficient. Rows (a) and (b) show the total count rates (DN per second per pixel) for the EI and NEI results, respectively. (c) shows the relative difference $(I_{\rm nei} - I_{\rm ei})/(I_{\rm nei} + I_{\rm ei})$ between the NEI and EI count rates.

contribution function that is calculated by using the ion fractions in the NEI states and the emissivities are calculated by using the emiss_calc package in the CHIANTI database. EM is the emission measure, assuming the line-of-sight (LOS) of 10^9 cm. The SDO/AIA effective areas are applied to get count rates in each AIA band. Finally, the AIA intensity that counts all emission lines from the above 14 elements is calculated at each cell of the MHD simulations.

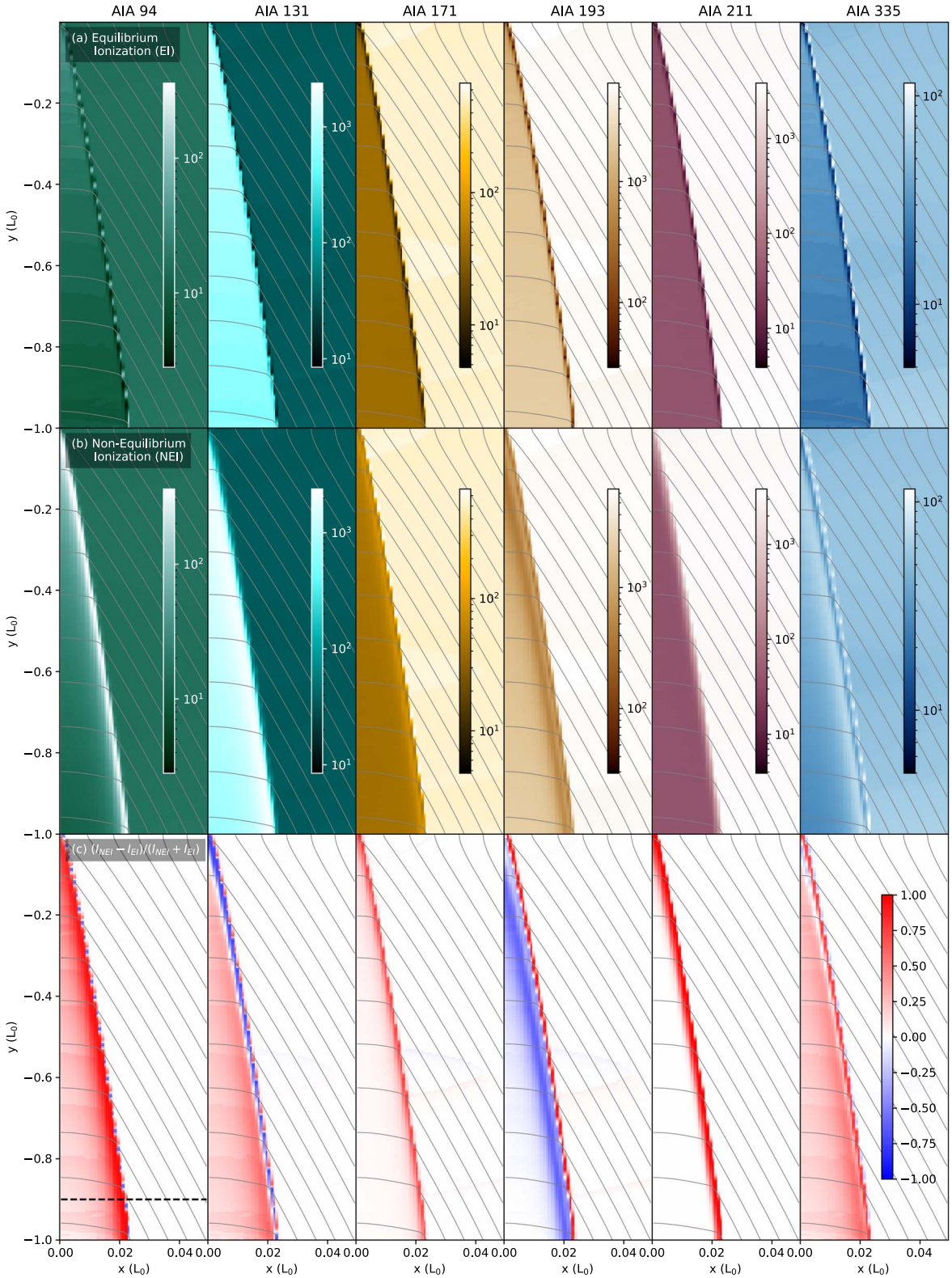

Figure 6. Synthetic SDO/AIA images for Case A2 applying conduction flux limitation. The panels are defined the same as in Figure 5.

Figure 5 shows the synthetic SDO/AIA count rate for Case A2* with the thermal halo structures outside the shock front. The first row shows the AIA intensities under the assumption of EI and the second row shows the results using the NEI results, respectively. Because the post-shock temperature is around 1.6×10^7 K (see Figure 1(b)), an overall feature is that the inside region of the reconnection current sheet appears bright on the high-temperature AIA channels, such as AIA 94 Å and AIA 131 Å, in both the NEI and EI cases. Other AIA channels show lower count rates in the current sheet than ambient plasma. Under the

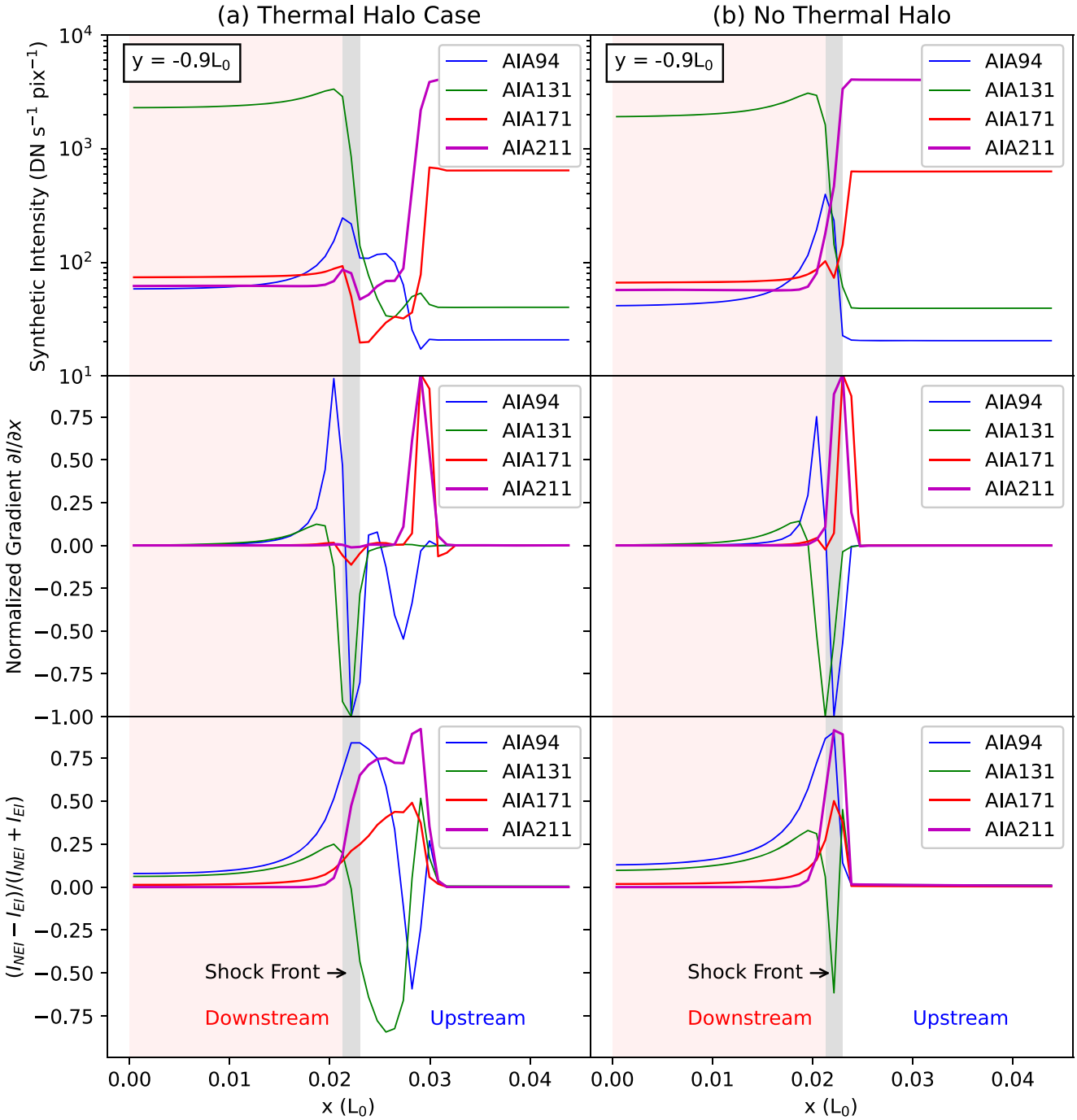

Figure 7. Synthetic SDO/AIA intensity in the NEI around the shock front along the horizontal sampling line at $y = -0.9L_0$ as shown by the dashed line in Figures 5 and 6. The left panels (a) represent Case A2* with the thermal halo, and the right panels (b) represent Case A2 without the thermal halo, respectively. The top rows denote the emission intensity (I), the middle rows the normalized intensity gradient in the x-direction $\partial I/\partial x$, and the third row the predicted intensity difference between the NEI and EI results, $(I_{\rm nei} - I_{\rm ei})/(I_{\rm nei} + I_{\rm ei})$.

assumption of EI, the thermal halo can be clearly recognized in all SDO/AIA channels because the emission intensity is only temperature dependent (Figure 5(a)). It appears as significantly low emission sheathes outside the Petschek-type shock fronts in the AIA 94, 171, 193, 211, and 335 Å channels. For the higher temperature AIA 131 Å channel, the thermal halo shows an extending bright edge around the shock fronts. However, the NEI synthetic images show that the signal of the thermal halo regions is significantly weaker than that under the assumption of EI. As shown in Figure 5(b), the low-emission sheath is hard to observe in AIA 131 Å, which causes a narrower bright reconnection region compared to the EI image in this channel. In contrast, the AIA 94 Å and AIA 211 Å maps generally show a wider bright reconnection current sheet region compared with the EI images due to the contribution of the effects of NEI on the thermal halo regions. We can see the effects of NEI on the intensities from the scaled relative difference $((I_{\rm nei} - I_{\rm ei})/(I_{\rm nei} + I_{\rm ei}))$ of the synthetic emission intensity between the NEI and EI cases (see the third row of Figure 5). Inside the reconnection region, the assumption of EI causes underestimated count rates in the AIA 94, 131, and

335 Å channels, but gives a higher AIA 193 Å intensity compared with the NEI results. Around the shock front and the thermal halo regions, the AIA 131 Å count rates under the assumption of EI are clearly overestimated compared to the NEI predictions, while those of AIA 171 and 211 Å are underestimated.

As a comparison, we show the synthetic SDO/AIA images in Figure 6 for Case A2 with the thermal conductive flux limitation. The underestimated AIA 94, 131, 171, and 335 Å features under the assumption of EI and the overestimated AIA 193 Å intensity are all the same as in Case A2*. Because there is no clear thermal halo in this model, the EUV intensity clearly jumps across the shock front as shown on most bands, such as AIA 171, 131, and 193 Å, due to both the temperature and density jumps. Furthermore, the NEI also causes an enhanced brighter edge close to the shock front on the post-shock side (Figure 6(b), (c)), which is generally brighter than that in the thermal halo regions. Unlike the thermal halo situation, the reconnection current sheet can be slightly narrower in AIA 211 Å due to the effects of NEI.

Here, we look into the details of emission from the thermal halo and shock front along a chosen sampling line at the height $y = -0.9L_0$ (as shown by dashed lines in Figures 5 and 6). Figure 7 shows the predicted intensity profiles for the AIA 94, 131, 171, and 211 Å bands. In the model with a thermal halo (Figure 7(a)), the intensity jump for the high-temperature channels, such as AIA 131 Å, mainly appears at the shock front (indicated by vertical gray shadows). On the other hand, the relatively low-temperature AIA channels (e.g., 171 and 211 Å) show clear jumps at the edge of the thermal halo region. The above intensity changes are more easily seen by plotting the normalized gradient profiles as shown in the second row of Figure 7. The dominant AIA 171 and 211 Å gradient peaks appear at the thermal front ($x \sim 0.03L_0$), while the negative gradient peaks of AIA 94 and 131 Å appear at $x \sim 0.023L_0$. In comparison, in the model without the thermal halo, all dominant AIA intensity jumps can be found at the shock front where the gradient peaks of AIA 94 and 131 Å are still negative, and those of AIA 171 and 211 Å are positive, respectively.

To further improve our understanding of how NEI affects the SDO/AIA intensity changes crossing the shock front, we plot out the relative difference between the NEI and EI in the third row of Figure 7. In the thermal halo case, under the assumption of EI, the AIA 171 and 211 Å intensities in both the downstream and thermal halo regions are underestimated, and AIA 131 Å in the thermal halo region is overestimated by more than a factor of 3. In conclusion, the analysis of different variations in the EUV intensity around the shock front serves as a potential diagnostic tool for understanding the shock properties. From the pre-shock plasma to the downstream of slow-mode shocks, one can expect the positive AIA 171/211 Å jump to be followed by a minimum value on the AIA 94/131 Å gradient. The gap between the two jumping peaks may indicate the halo region.

It is interesting to analyze how the NEI affects the plasma temperature derived from images in the above six SDO/AIA channels. In general, the EM reconstruction method is used to investigate the plasma temperature and density in high-temperature plasma during solar eruptions. The differential emission measure (DEMs) can be calculated from the intensities of six SDO/AIA channels (94, 131, 171, 193, 211, and 335 Å) that are dominated by emissions from iron lines and other elements (O'Dwyer et al. 2010), and the DEM-weighted average temperature can be used to estimate the temperature of the reconnection current sheets. However, the NEI may cause a significant departure in the DEM-weighted temperature from the *real* plasma temperature. We, therefore, perform a DEM analysis based on the above synthetic AIA images and make detailed comparisons in different cases.

In observational studies, the DEM-reconstructed temperature strongly depends on the multiple temperature model, which may cause slightly different results with different solvers (e.g., Cheung et al. 2015; Szenicer et al. 2019). In our case, the modeled synthetic SDO/AIA intensity can be thought of as a *single-T* component profile: it is integrated along the z-direction where the temperature is assumed to be uniform along the LOS. The DEM distribution can be obtained by using the *single-T* approximation. We then simply estimate the reconstructed temperature $T_{\rm nei}$ according to the χ^2 minimization method by setting

$$\chi^2(x, y, T) = \sum_{i=1}^{6} (I_{\rm nei}(x, y)_i / n_e(x, y)^2 - I_{\rm ei}(T)_i)^2. \quad (22)$$

Here, $I_{\rm ei}(T)_i$ is the intensity of the ith channel among the six AIA bands with the unit plasma density under the assumption of EI, and n_e is the density in the MHD models.

Figure 8 compares the reconstructed temperature distribution with the MHD-modeled temperature in three cases. Figures 8(a) and (b) show Cases A2 and A2* where the shocked plasma is heated to $\sim 1.6 \times 10^7$ K with a density higher than $\sim 10^{10}$ cm^{-3}, and Figure 8(c) is for the relatively lower temperature ($\sim 10^7$ K) and density ($\sim 2.5 \times 10^9$ cm^{-3}) situation in Case B3. Consistent with the above NEI analysis, the under-ionized feature inside the reconnection current sheet causes a significant underestimation of the EM reconstructed temperature. As shown in the temperature maps in Figure 8, the high-temperature plasma sheet appears narrower than the actual high-temperature plasma sheet in all three cases. Solid red lines clearly show the lower reconstructed temperature along the horizontal sampling lines. We also plotted the relative difference $((T_{\rm NEI} - T_{\rm EI})/T_{\rm EI})$ between the reconstructed temperature ($T_{\rm NEI}$) and the real one ($T_{\rm EI}$) in the right panels in Figure 8. The relative difference can be as high as 60%, which occurred near the shock front. The orange dots mark the location where the reconstructed temperature is noticeably lower than the actual temperature, ~20% at $x \sim 0.017$ in Case A2 (and A2*) and $x \sim 0.015$ in Case B3. In Figure 8, The red dots mark the edge of a high-temperature current sheet by using the half-maximum temperature, and the distance between two red dots from the NEI and EI profiles is shown by Δx accordingly. We can see that the apparent width of current sheets may be narrower than their actual width by about 8%, 31%, and ~36% according to the emission reconstruction method in the above Cases A2, A2*, and B3, respectively.

An expanding halo region can be found in Case A2* shown in Figure 8(b). The reconstructed low-temperature edge comprises two parts: the thermal halo region due to thermal conduction and the lower $T_{\rm NEI}$ regions due to the NEI. Compared with Case B3 (without the thermal halo), it is interesting that both reconstructed low-temperature edges show very similar distribution features. Therefore, the diagnostic of shock structures and possible thermal halos on high-temperature emission requires a detailed analysis of the effects of NEI.

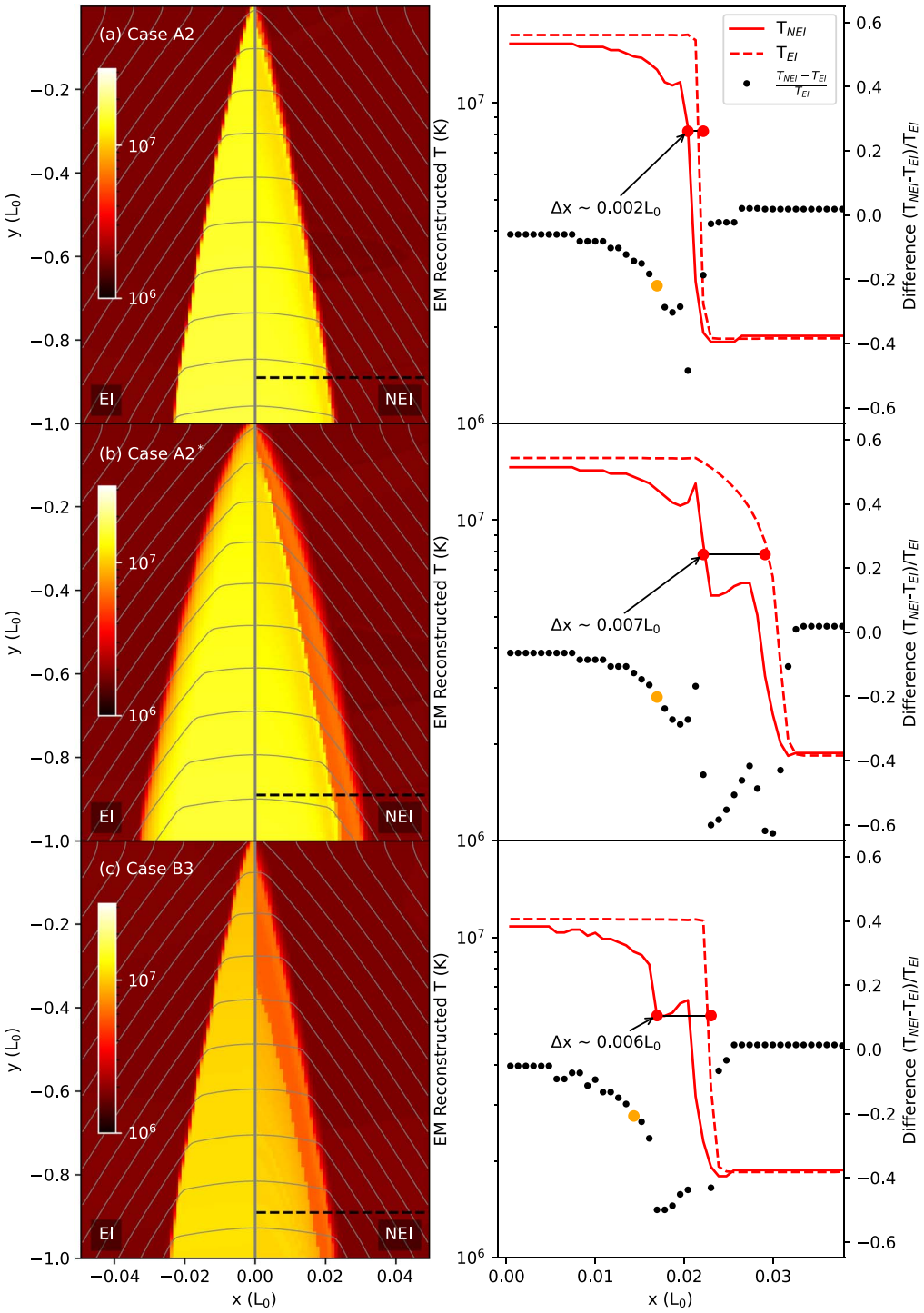

Figure 8. EM reconstructed temperature distribution using the synthetic SDO/AIA intensity for Cases A2, A2*, and B3. In each temperature map, the left region (x ranges from -0.05 to 0) shows the MHD-modeled temperature (or temperature in the EI), and the right part (x ranges from 0–0.05) is for the reconstructed temperature. The right panels show the temperature distribution, and the relative difference between the NEI and EI results along the horizontal sampling line at $y = -0.9L_0$ (dashed black lines on the left panels). The two red dots mark the location of the half-maximum temperature, and Δx indicates the distance between the above two red cycles in the x-direction. The orange dot indicates the position with an ~20% difference along the dotted lines.

3.4. Reconnection Current Sheet above the Closed Loops

In this section, we perform a more realistic simulation following the configuration of the classical solar flare model (e.g., Kopp & Pneuman 1976). In this case (see the detailed simulation parameters in Table 1, Case D), we apply a similar setup except introducing gravity in the y-direction, and utilizing the line-tied boundary condition at the bottom to ensure that the magnetic field lines are rooted on the solar surface. Driven by the initial perturbation on magnetic fields (e.g., Shen et al. 2018), the magnetic reconnection quickly takes place in the initial current sheet, and a pair of reconnection outflows appear along the vertical direction (y-) the same as in Case A2. However, the reconnected magnetic flux gradually accumulates at the bottom due to the line-tied condition, and the closed

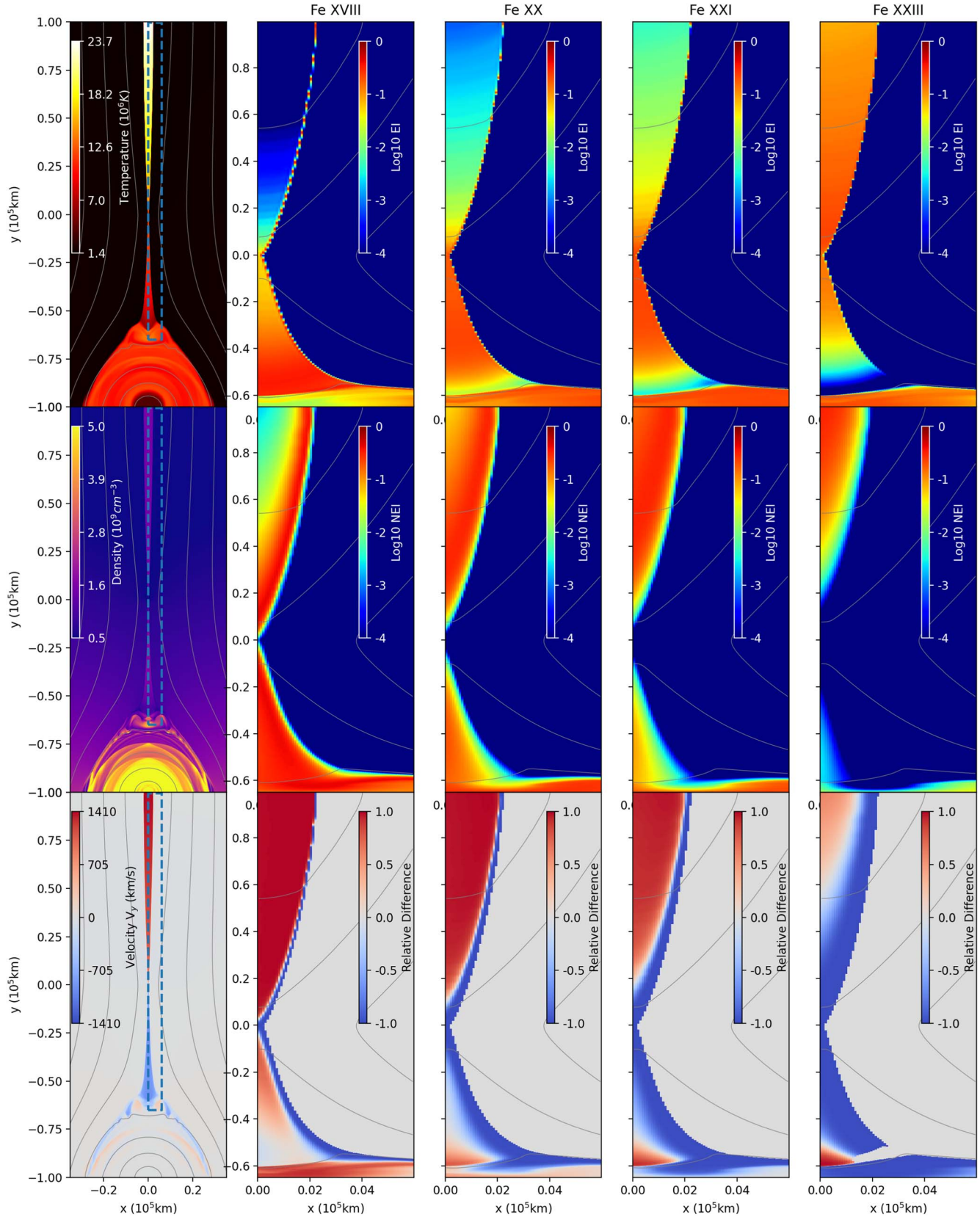

Figure 9. Ionization distribution with the line-tied boundary condition in Case D. The left panel shows the distributions of temperature, density, and velocity component V_y at the time $t = 16t_0$. The right panels illustrate the ion fraction of Fe XVIII, Fe XX, Fe XXI, and Fe XXIII in the local region shown by the blue box on the left panels. The top row shows the ion fractions in the EI (f_{ei}), the second row is for the NEI (f_{nei}), and the third row shows the relative differences between the NEI and EI defined by $(f_{nei} - f_{ei})/(f_{nei} + f_{ei})$.

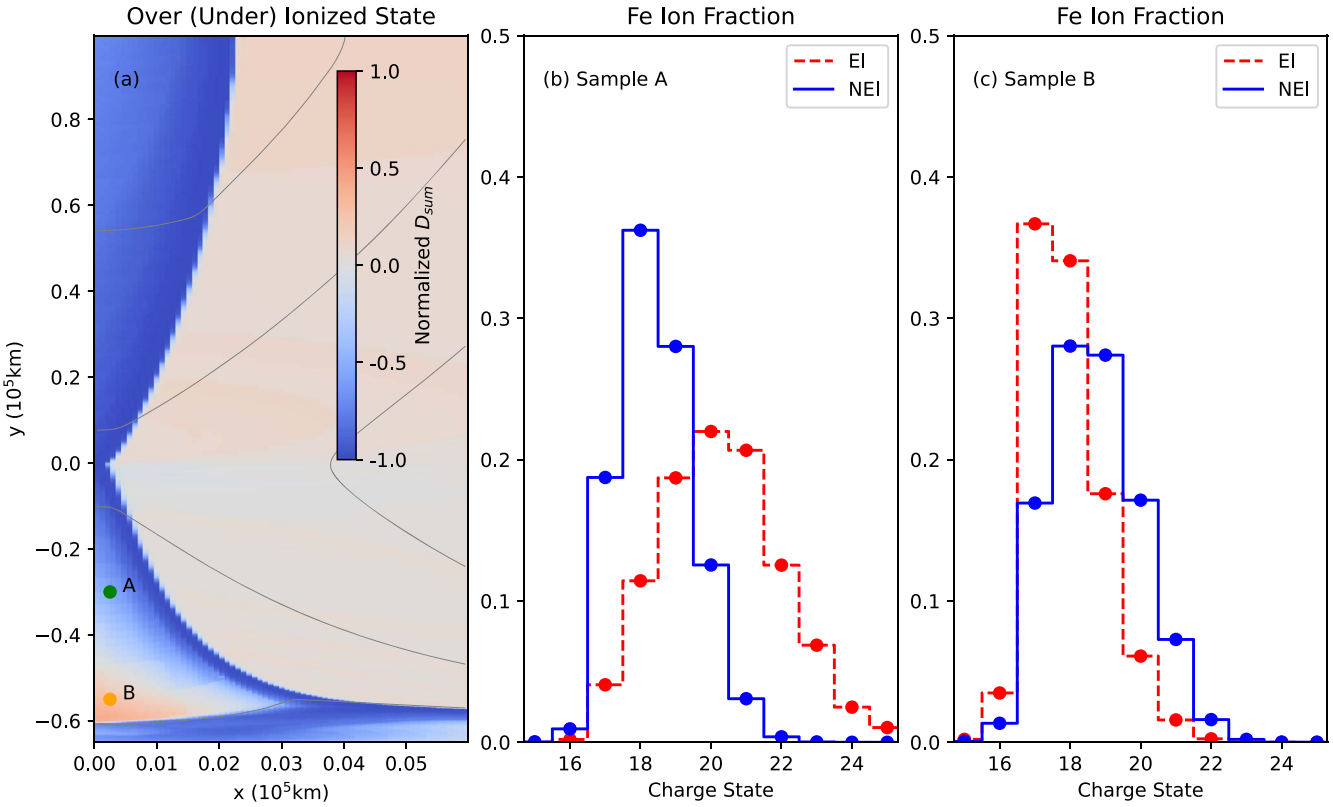

Figure 10. Under-ionized and over-ionized ionization states in the downward outflow regions. Panel (a) shows the normalized total difference ($D_{\rm sum}$) between the NEI fraction and the assumption of EI; (b) and (c) show Fe ion populations at two chosen sampling points indicated by green and orange cycles in panel (a), respectively. An animation of this figure is available in the online journal. The left panel shows the normalized total difference ($D_{\rm sum}$) between the NEI fraction and the assumption of EI. The right panel shows the Fe ion populations at the chosen sampling point indicated by the white dot in the left panel. This movie illustrates that as the selected sampling point moves from the low tip of the reconnection current sheet to higher altitudes, the ion charge state distribution in the NEI (blue line) skews from higher charge states to lower charge states, compared to the EI results (red line).

(An animation of this figure is available.)

magnetic loops appear at the bottom representing the flare loops. In this case, the downward-moving outflow collides with the newly closed magnetic loops and may form termination shocks if the outflow speed exceeds the local fast-magnetosonic speed in the loop-top region (Forbes 1986). In general, these closed magnetic loops also cause asymmetrical reconnection outflow behaviors along the reconnection current sheet: the downward outflow generally has lower speed compared with the upward one. Therefore, the ionization states could be significantly different along the reconnection current sheet.

Figure 9 shows the spatial distribution of the primary plasma variables (temperature, density, V_y) and the ion fractions of selected Fe ions in the reconnection current sheet and flare loops regions. At this time ($t = 16t_0$), the reconnection evolved into the relatively steady phase when the flare loops had already fully developed. As the same as in the other cases in Table 1, the enhanced resistivity diffusion center is still located at the system center ($[x = 0,\ y = 0]$) at which the primary reconnection X-point can be found. Bidirectional high-temperature reconnection outflows are displayed in the left panels of Figure 9. Here, the upward outflows can reach 2×10^7 K with the maximum flow speed exceeding 1400 km s^{-1}. On the other hand, the temperature of the downward reconnection jet is as low as $\sim 10^7$ K and its velocity is relatively slow ($\sim$800 km s^{-1}). Under the assumption of EI, high ionization ions (e.g., Fe XXIII) should mainly dominate the upward outflow due to the extremely high temperature, and more Fe XVIII and Fe XX ions could appear in the downward outflows because of the slightly lower temperature as shown in the top row of Figure 9. However, we will discuss how the actual ion distribution is different from the assumption of EI.

The effect of NEI can cause substantial departures of the ion distribution from the EI states in both the upward and downward outflow regions, shown in the second row of Figure 9. Consistent with the above discussion of Petschek-type reconnection configurations (e.g., Figure 3), the upward flow displays clearly under-ionized features. The populations of Fe XVIII, Fe XX, and Fe XXI in the NEI are all substantial in the upward outflow regions compared with the assumption of EI in which, for instance, the Fe XVIII is rare. The difference in the ion fraction between the NEI and EI can be large, as shown in the third row of Figure 9. For example, the maximum relative difference of Fe XVIII is close to one along the upward reconnection flow. The Fe XXIII also shows the same behavior, except a slightly negative difference appears in the edge region inside the current sheet.

Along the downward reconnection jet, the ionization state is more complex than the ideal Petschek-type reconnection current sheet due to the dramatic variation of both temperature and density with height. As shown in Figure 9, the plasma temperature is high near the reconnection X-point, but quickly decreases near the lower tip of the reconnection current sheet because of the expansion of the outflows in the horizontal direction. The relatively low-temperature plasma continually

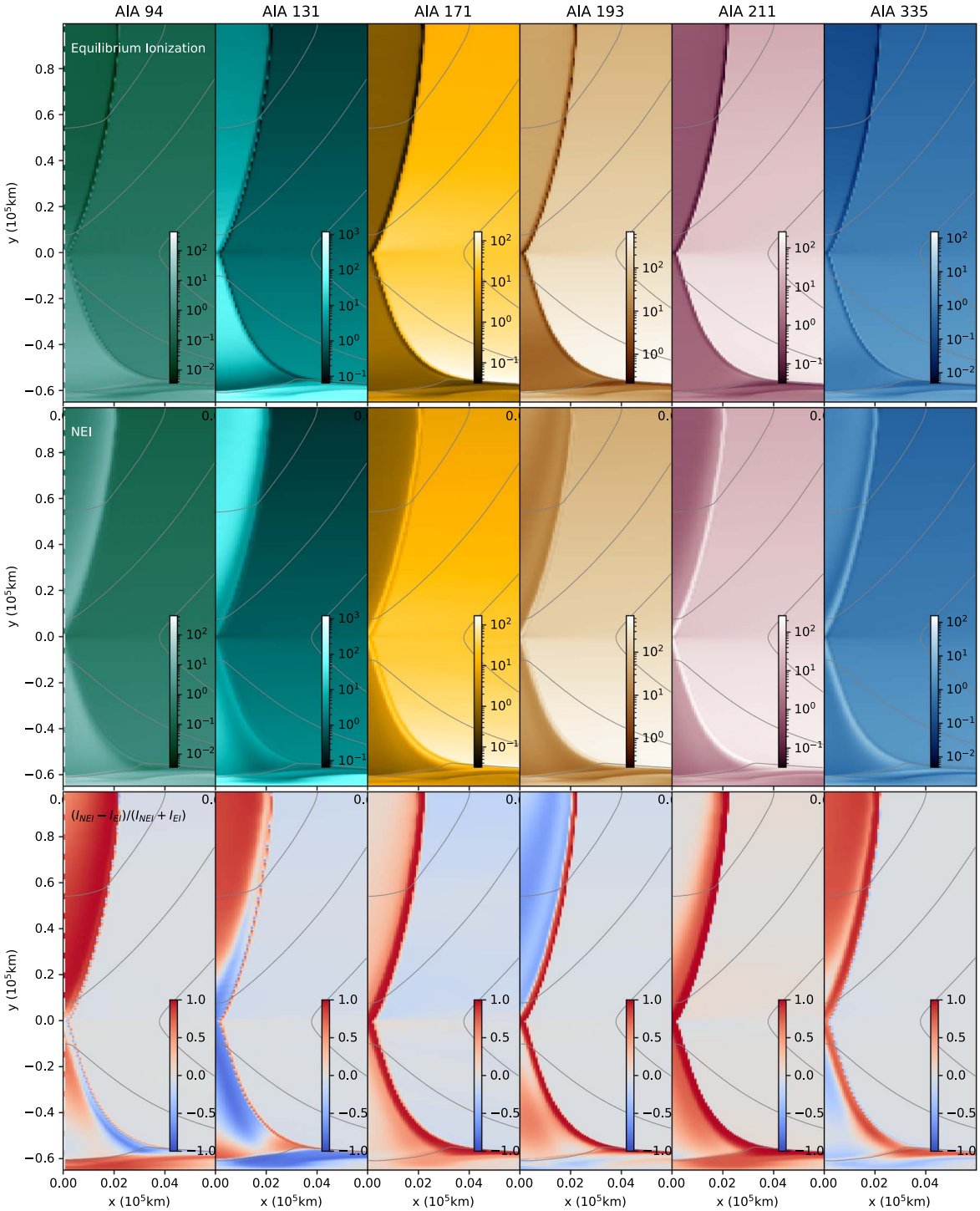

Figure 11. Synthetic SDO/AIA images in Case D applying the line-tied boundary at the bottom. The first row shows the AIA count rates under the assumption of EI, and the second row shows the NEI results. The third row shows the relative difference between the NEI and EI results.

outflows downward until it collides with the closed magnetic loops, where the outflow speed drops substantially. In the situation including super-magnetosonic reconnecting outflows, the plasma can be quickly heated again behind the termination shock. The above temperature variation then causes two different types of NEI states: (i) near the X-point, the plasma is under-ionized, the same as in the classical Petschek-type reconnection current sheet (e.g., the upward reconnection jets in this model); (ii) the plasma could be in over-ionized states due to the rapid temperature drop at the lower tip of the downward flows. As shown in the third row of Figure 9, the relative difference in Fe XVIII appears as clearly negative values (indicated by blue colors) at the lower end of the reconnection downflows while the other three higher ionized ions become more abundant.

The reversal between under-ionized and over-ionized states can clearly be seen in Figure 10. We introduce the normalized total difference of ion fraction to show the departure of the NEI

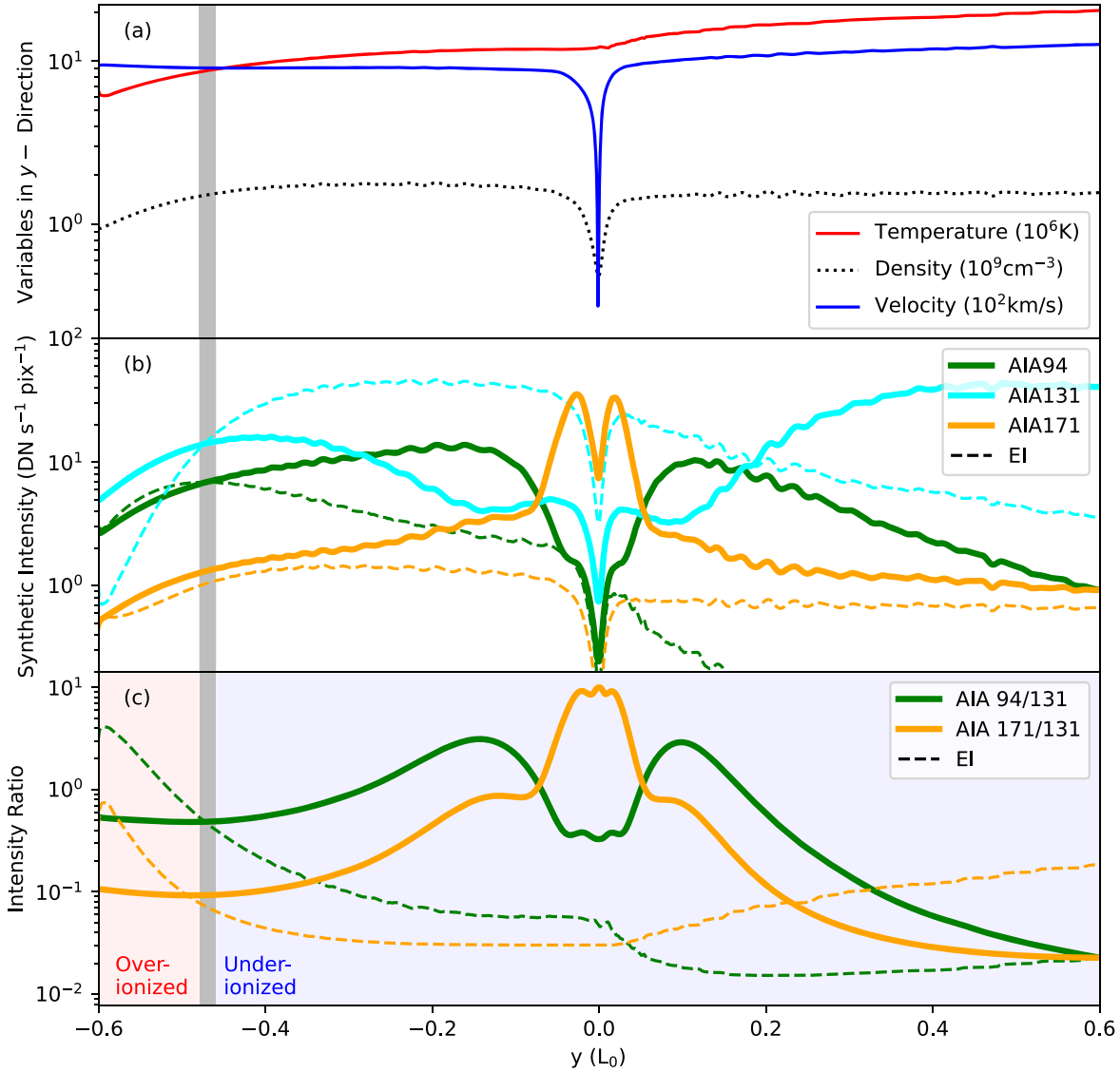

Figure 12. Synthetic SDO/AIA intensity and primary variable distributions along the reconnecting current sheet in Case D. (a) Temperature, density, and velocity profiles along the white vertical sampling line in Figure 11. The vertical gray-shaded region indicates the position where the ionization property of the reconnection current sheet changes from under-ionized to over-ionized states. (b) The chosen SDO/AIA count rate profiles. The bold lines denote the NEI results and the dashed lines denote the assumption of EI. (c) Intensity ratios, AIA 131/94 Å and AIA 131/171 Å for both the NEI and EI calculations.

from the EI, defined by

$$D_{\rm sum} = \sum_{1}^{i_{\rm equal}} - \frac{(f_{\rm nei} - f_{\rm ei})}{2} + \sum_{i_{\rm equal}+1}^{Z+1} \frac{(f_{\rm nei} - f_{\rm ei})}{2}. \quad (23)$$

Here, $f_{\rm nei}$ and $f_{\rm ei}$ are the ion fraction of the ith charge state in the NEI and EI cases, Z is the atomic number of the chosen element to be calculated, and $i_{\rm equal}$ is used to point to a particular charge state where the nonzero NEI fraction is equal (or closest) to the EI fraction. In this way, $D_{\rm sum}$ can range from -1 to 1 depending on the ionization state. Under-ionization causes a negative $D_{\rm sum}$ value, and $D_{\rm sum} > 0$ is for the opposite case when the dominant NEI fractions are larger than the EI in over-ionized states. Figure 10 and animation (a) show the $D_{\rm sum}$ distribution of Fe ions around the reconnection current sheet. The upward outflow is dominated by negative $D_{\rm sum}$ due to the under-ionized plasma, while the under-ionized state could change to the over-ionized state at the low tip of the reconnection current sheet. Two sampling points (A and B in Figure 10(a)) are chosen to show the Fe ion fraction profile at different heights. As shown in panels (b) and (c) in this figure, the ion charge state distribution in the NEI (solid line) is skewed toward lower charge states compared to the EI results (dashed line) at the upper sampling point A, and shifted to higher charge states at the lower sample B.

Figure 11 shows the predicted SDO/AIA count rate images from the above modeling with the line-tied boundary. The first row shows the EI results, and the second row shows the intensities of the NEI calculations, respectively. Similar to the classical Petschek-type reconnection current sheet, the NEI causes stronger emissions in upward outflows regions in the AIA 94, 131, 171, 211, and 335 Å channels. The largest relative difference between the NEI and EI count rates appears in the AIA 94 and 131 Å channels, which are close to unity inside the current sheet. In downward outflows, either higher or weaker NEI count rates can be found at different heights. In the AIA 94 Å map, the reversed ionization charge states at the

lower tip of the current sheet also cause weaker emission (as shown by blue colors in the third row of Figure 11).

Figure 12(a) shows the variation in the count rates of the chosen high-temperature SDO/AIA bands (AIA 94 and 131 Å, Figure 17) along the reconnection outflow direction (also see the white vertical-dashed lines in Figure 11, left panels). In upward outflows ($y > 0$), the temperature gradually increases from $\sim 1.2 \times 10^7$ to $\sim 1.8 \times 10^7$ K while the density slightly decreases as the plasma flows to a higher altitude from the reconnection X-point because the ambient coronal density decreases with the height due to the gravity (Figure 12(a)). The AIA 94 and 131 Å count rates in the EI dramatically decrease at the high-temperature end due to temperature (and partly density) variations, as shown in Figure 12(b). The AIA 171 Å map maintains relatively lower count rates because of the low-temperature response in the high-temperature ranges (e.g., $\log(T) > 6.8$ K, in Figure 17), and its variation along the y-direction is more dominated by the density distribution. In contrast, the AIA 131 Å intensity in the NEI increases away from the reconnection X-point, due to the under-ionization. In addition, AIA 94 and 171 Å count rates are all significantly enhanced in the NEI calculations compared with the EI results. The under-ionization of the current sheet also causes different features in different AIA intensity ratio profiles. Figure 12(c) shows the ratios of the brightest lines: AIA 94/131 Å and AIA 171/131 Å. For comparison, we also plot these ratios in the EI cases using dashed lines. Because the effect of NEI causes enhanced AIA 131 Å emissions in the reconnection upflow regions where the temperature increases with the height, the AIA 171/131 Å ratio (orange line) in the NEI decreases as the reconnection current sheet temperature continually increases to 1.8×10^7 K, which is reversed from the AIA ratio (Figure 17) based on the EI. The AIA 94/131 Å ratio is also notably higher than the AIA 171/131 Å ratio, due to the effects of NEI.

In downward outflow regions, the temperature is relatively lower compared with the upward outflows, and the density drops near the low tip of the reconnection current sheet. Under the assumption of EI, the AIA 94/131 Å and AIA 171/131 Å ratios are expected to increase at the low tip of the reconnection current sheet, when the temperature drops to $\sim 6 \times 10^6$ K. However, the over-ionization greatly diminished this tendency as shown by the red shadowed regions in Figure 12(c). The NEI AIA 94/131 Å (and AIA 171/131 Å) ratios are then less than those under the assumption of EI about one order of magnitude at $y \sim -0.6L_0$ accordingly.

3.5. Radiative Cooling in the NEI

Optically thin radiative cooling can be affected by the NEI when the ion population significantly departs from the assumption of EI. Once the NEI population is known, the radiative loss rate can be directly calculated by summing over all the transitions for all abundant ions. In solar coronal environments, the dominant radiative process includes bound–bound emission, while free–free, bound-free, and two-photon transitions also make significant contributions to high (and low) temperature plasma. So, we consider the above four transition processes in the following calculations. Because the radiative emissions are functions of electron temperature but are less sensitive to density (aside from the proportionality to ρ^2), we neglect the density dependence and assume the electron density is 10^9 cm^{-3} in the current analysis. However, it should be easy to include wider density ranges in these particular calculations.

In order to combine the NEI cooling into the MHD simulation, the total change in energy density due to optically thin radiative cooling can be described in the following form:

$$\frac{\partial E}{\partial t} = -\rho^2 \Lambda(T, f_i). \tag{24}$$

Here, E is the total energy density, ρ is the plasma density, and $\Lambda(T, f_i)$ is the total radiative cooling rate, which is the function of temperature (T) and ion fractions (f_i). We calculate the cooling rate for each ion charge state, including the above four transition processes without an ion fraction and the assumption of abundance Thus, the total cooling rate $\Lambda(T, f_i)$ can be updated with the ion fraction either in the NEI or EI in the form of

$$\Lambda(T, f_i) = \sum_{\text{elements}} \text{Abund} \times \Big(\sum_{\text{charge states}} f_i \times \text{RadLoss}_4(T) \Big), \tag{25}$$

where Abund is the element abundance, f_i is the ion fraction of the ith charge state based on NEI (or EI) calculations, and $\text{RadLoss}_4(T)$ is the cooling rate, including the free–free, bound-free, bound–bound and two-photon emissions obtained from the CHIANTI database (Dere et al. 2019) on a temperature grid. In cases where f_i is set to be the EI fractions, the total $\Lambda(T, f_i)$ will be the same as the one in the CHIANTI database (solid blue circles in Figure 13).

In the combined MHD-NEI simulations, the radiative loss rate Λ is computed by interpolating on temperature grids using local NEI ion fractions. This can be separated into the temperature-dependent cooling functions and the ion fractions, and be used in either one-step integration with time or multiple time-step schemes in an MHD solver. In this particular MHD-NEI simulation, one may not include all elements in the NEI module. So the cooling rate Λ can be modified only for several abundant elements with the updated NEI fractions, and all other rates are approximated under the assumption of EI. For example, in the high-temperature coronal plasma (10^6 K $\sim 10^7$ K), the most critical elements for cooling loss are Fe, Si, Mg, and O, as shown in the right panel of Figure 13.

As shown in Equation (25), the radiative cooling is proportional to ρ^2, so the cooling affects the high-density plasma, where the impact of the NEI will be diminished. In general, radiative cooling is expected to be smaller than expansion or thermal conduction cooling in high-temperature magnetic reconnection regions. In addition, radiative cooling is very important in the cooler, denser prominence cores of CMEs, but the high density will limit the differences between the EI and NEI. However, due to the under-ionized nature inside Petschek-type reconnection current sheets, the systematic departure of cooling rates between the NEI and EI in reconnection outflows may still affect the long-term evolution of the magnetic reconnection configuration.

Therefore, we compare two runs with different cooling rates using similar parameters based on Case A2. In the two runs, the cooling term $-\rho^2 \Lambda(T, f_i)$ has been added into the energy equation, Equation (4). Because of the radiative cooling terms, the temperature of the background plasma could continually decrease to be much lower than the initial values. However, in order to obtain reasonable ionization states in the background corona, the upstream plasma should be in (or be close to) the typical corona temperature (e.g., 2 MK). Therefore, to balance

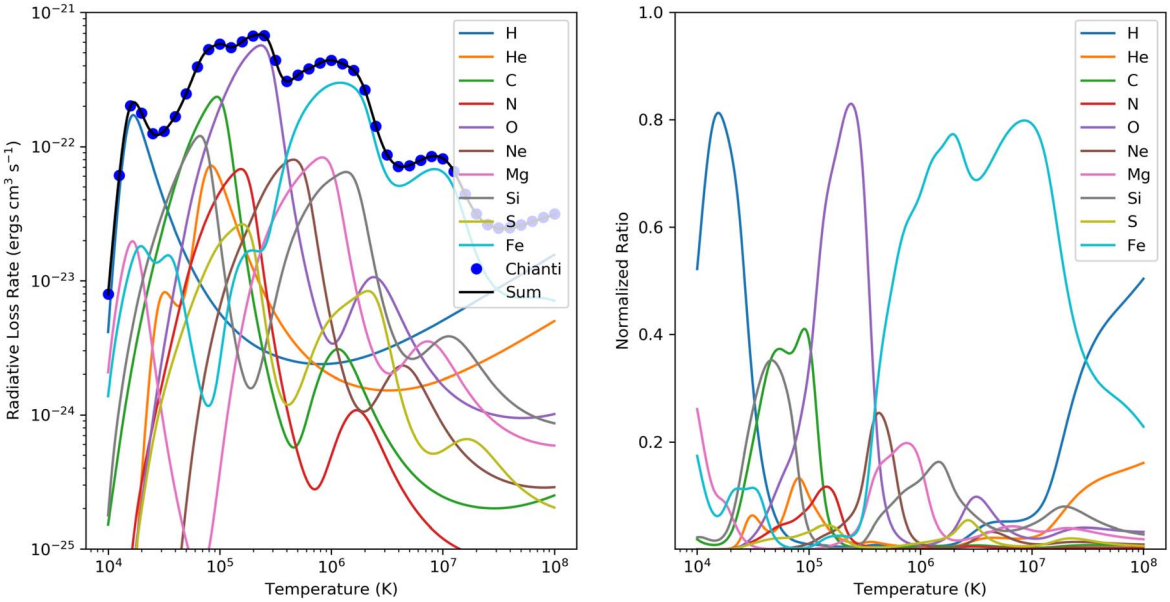

Figure 13. Left panel: the radiative cooling rate of 10 abundant coronal elements saved in the table. The rates are calculated using the CHIANTI database (version 9). In this plot, we use the elemental abundance from the compilation by Schmelz et al. (2012), and all ion fractions are assumed to be in the EI. Right panel: the relative contribution of each element on the total loss rate based on the same assumption as that in the left figure.

the energy loss due to the radiative cooling, we included an artificial corona heating term (ρH_0) in the source term, $S = \mu_0 \eta_m j^2 + \nabla_\parallel \cdot \kappa \nabla_\parallel T + \rho H_0 - \rho^2 \Lambda(T, f_i)$. Here, H_0 is a constant heating rate defined by temperature so that ρH_0 balances the radiative cooling term at the beginning. In Figure 14, the solid lines illustrate the case employing the cooling rate from the NEI results, and the dashed lines denote the cooling rates based on the assumption of EI. An overview feature is that the NEI cooling rates cause a slightly hotter reconnection outflow. Inside the current sheet, the largest difference in temperature between the EI and NEI cooling is around ~5%. Meanwhile, the outflow speed in the NEI case is slower than that in the EI. However, the chosen Fe ion fraction is basically the same in the two runs, with a difference of $f < \sim 2\%$. We noticed that the primary variable profiles (including T, ρ, and v) show some rippling perturbations with height, due to the numerical issues driven by the initial unbalance between heating and cooling once the magnetic reconnection occurs at the reconnection X-point at the beginning. However, these ripples are small, and we can still obtain the long time tendency of the effects of NEI on the reconnection configurations. Thus, the effect of NEI cooling is negligibly small in the analysis of Fe ion populations during short reconnection events (e.g., a few Alfvén times). On the other hand, NEI cooling also contributes to the temperature and density structures and should be further considered, especially in long-duration MHD simulations.

4. Discussion

The magnetic reconnection is expected to significantly affect the temperature distribution along the reconnection current sheet. In reconnection theories, the competing heating mechanism includes Petschek shock heating, multiple X-points and plasmoids, and turbulent heating, which may cause entirely different ionization features. In the Petschek shock configuration, the layered feature of ionization is reported in recent studies (e.g., Imada 2021; Imada et al. 2011). However, the heating due to multiple small-scale plasmoids and/or small-scale short-lived heating regions in turbulent reconnection (Lazarian & Vishniac 1999) may cause more complex ionization features. In recent numerical modeling, several types of research suggest that those differences can simultaneously appear in large-scale reconnection current sheets (e.g., Mei et al. 2012). Therefore, high-resolution MHD-NEI modeling is required to make meaningful comparisons with the observations.

As mentioned in the previous sections, a Maxwellian distribution of electrons is assumed in our current models. The ionization and recombination rates, as well as the ionization states, are all based on this assumption. However, a significant fraction of electrons in the flare reconnection region can be accelerated into a power-law energy spectrum. Such energetic particles can significantly affect the ionization/recombination processes. For example, if the nonthermal electron distribution contains excess particles at about 5–10 times the mean energy, they can significantly increase the ionization rates. The effect of NEI may be enhanced around the shock front, where the electrons include nonthermal tails. Therefore, future studies should include both time-dependent ionization and nonthermal particles to obtain more accurate results for diagnostic studies of erupting plasma.

Our current model is based on single-fluid MHD simulations. In particular, the element abundance is assumed to be uniform in the whole simulation domain. However, in realistic large-scale models of solar eruptions, the reconnection inflows around the reconnection current sheet may come from lower altitudes (e.g., Shen et al. 2013b), where the plasma could already mix with chromosphere components. The background element abundance around the reconnection current sheet should be obtained by considering the entire history of plasma flowing. Thus, the element abundances of the current sheet might evolve, affecting the optically thin radiative cooling calculations and the predicted EUV emission. Therefore, a further study of the ionization calculation based on a multi-fluid model will be required.

The importance of thermal conduction in reconnecting current sheets has been commonly recognized in both analytic and

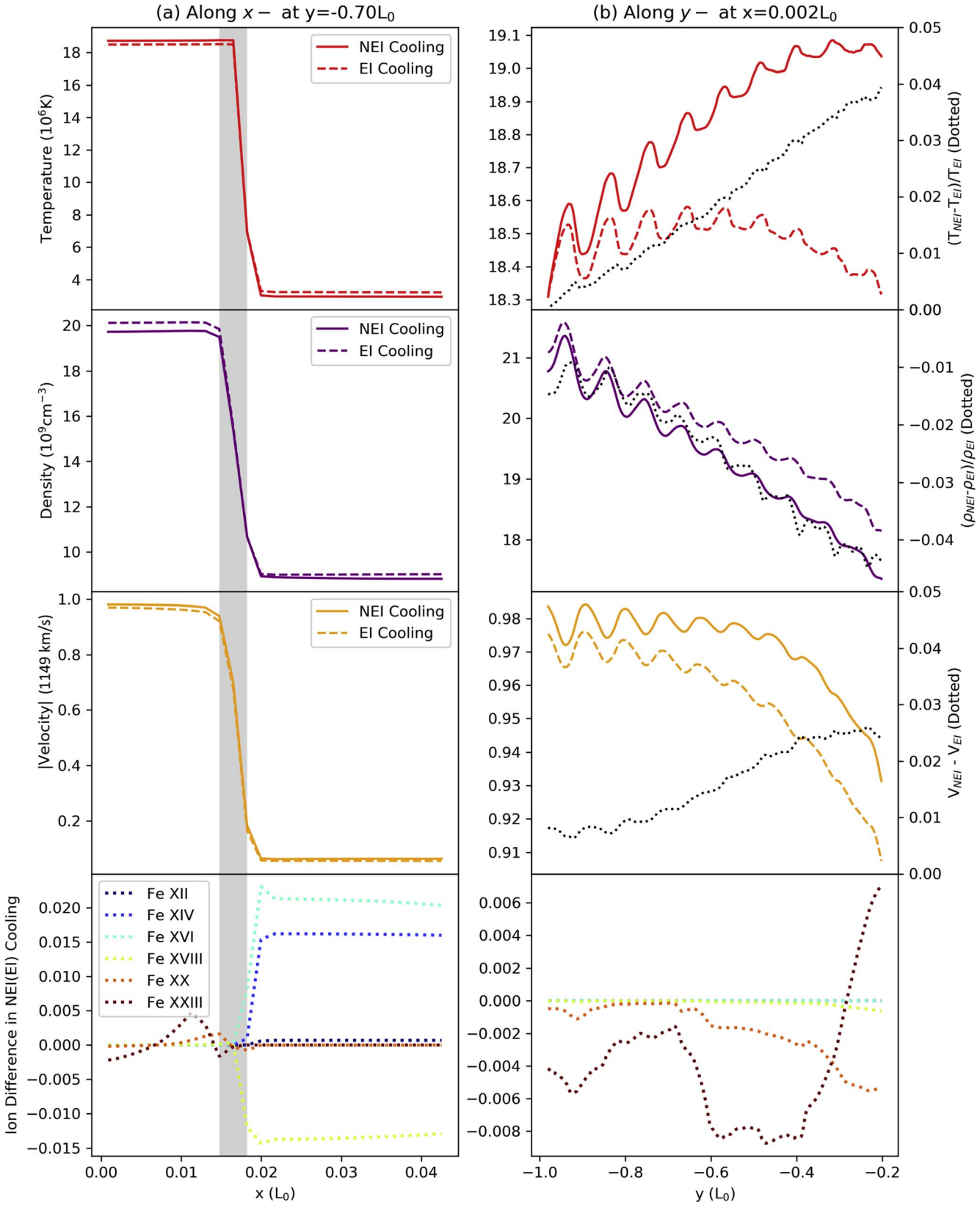

Figure 14. Comparison of the primary variables and ion charge states between the NEI-dependent radiative cooling case (solid lines) and the EI-dependent cooling (dashed lines). (a) Temperature, density, and plasma flow velocity along the reconnection inflow direction (x-) at $y = -0.7L_0$. The vertical gray shadows indicate the position of the shock front, and the reconnection X-point is located at $[x = 0, y = 0]$ as discussed in Figure 1 above. The bottom panel shows the differences in the Fe ion fraction defined by $f_{i,\mathrm{NEI\ cooling}} - f_{i,\mathrm{EI\ cooling}}$. (b) Similar to (a) but along the reconnection outflow direction (y-) at $x = 0.002L_0$. The right axis of each panel shows the differences between the two cases for temperature, density, and velocity profiles, respectively.

numerical models (e.g., Yokoyama & Shibata 1997; Chen et al. 1999; Yokoyama & Shibata 2001; Reeves et al. 2010). However, direct measurements of the conduction rates around the reconnection current sheet during solar eruptions are rare. In a 3D solar eruption model, Reeves et al. (2019) performed an energy budget analysis around the post-CME reconnection current sheet, and predicted synthetic XRT and SDO/AIA images. They found that thermal conduction transports thermal energy away from the current sheet region, and widens the region of high temperatures. On the other hand, the *thermal halo* may not be easily identified in realistic SDO/AIA observations, due to instrumental limitations. Seaton et al. (2017) performed a DEM analysis and revealed a highly uniform, hot current sheet with a cooler background. These results suggested that if the thermal halo is present, it is either too faint or too narrow a region to be detected in this eruption event. As discussed in these research studies, the thermal halo could even be contained entirely within the reconnection current sheet regions or become important near the tip of the current sheet above the flare loop tops. In either case, the analysis of the NEI around the reconnection current sheet should serve as a necessary tool for understanding the nature of thermal energy transportation across the slow-mode shock front.

It is worth estimating the computational cost of the in-line NEI module during MHD simulations. As mentioned above, we employ the passive scalar of the mass equation (Equation (1)) to store and update the ion population in the current calculation. Therefore, the required computer memory entirely depends on the number of ions to be solved. For instance, the MHD code saves at least 14 physical variables in memory for each cell (e.g., eight essential conserved variables, three interface magnetic fields, and three resistivity coefficients). In a particular model only including the Fe ions, the total number of ionization fractions occupying computer memory is around 2 times that of the original MHD variables. However, the cost may become more extensive by including all 14 abundant elements, which should be solved using multiple parallel cores and memories during simulations. Our calculations also show that the run times of the combined MHD-NEI modeling will be comparable with pure MHD simulations for the most abundant elements (e.g., C, O, or Fe). For instance, the model with 27 Fe ions spent ∼1.8 times the computer time compared with the pure MHD simulation with the same spatial resolution. In our cases, the massive runs, including all 14 elements, take about 7 times longer than the Fe-only calculation. However, it is noticeable that the above run-time estimations are also significantly affected by the chosen MPI communication module on the cluster computer.[2] Therefore, the run time could be decreased in the future in a more high-efficiency communication environment (e.g., a shared-memory machine). Thus, with only a modest increase in computing resources, NEI information will be conveniently achievable with available computing resources and allow for a new level of accuracy in diagnostic predictions. The NEI module used in this work has been made available to the public and can be freely obtained from the web.[3] The eigenvalue and eigenvector tables associated with updated ionization/recombination rates, and cooling rates are also collected in an open-source program.[4]

[2] Smithsonian High-Performance Cluster: https://doi.org/10.25572/SIHPC.
[3] NEI module: https://doi.org/10.5281/zenodo.6555135.
[4] NEI tables: https://github.com/ionizationcalc/time_dependent_fortran.

5. Conclusion

Using the combined MHD and NEI simulations, we analyze the Petschek-type magnetic reconnection current sheet and ionization charge states in solar corona environments. Based on the NEI results, we also predict the emission features observable by EUV instruments (SDO/AIA) for both ideal Petschek-type slow-mode shocks and solar flare reconnection current sheets.

NEI is essential for making accurate, self-consistent predictions of emissions from high-temperature plasma during a solar eruption. In this work, we incorporated a robust NEI solver (Shen et al. 2015) into the well-developed MHD code, Athena (Stone et al. 2008), to perform in-line MHD-NEI simulations. The solver can then solve time-dependent ionization equations in each time step during the MHD simulation and obtain information on evolving ion charge states on the whole simulation domain. We employ this method in several test projects, such as shock tubes (see Appendix A). Comparison with the post-processed NEI calculations shows that this in-line NEI module calculates charge states accurately, and it can be used in complex problems such as shocks and magnetic reconnection outflows. We then employed the above method in the Petschek-type magnetic reconnection configuration. We obtained the NEI properties for both the classical Spitzer thermal conduction and conductive flux-limited models. The features of the NEI and EUV emission around the reconnection current sheet are studied and summarized.

1. The high-temperature thermal halo around the Petschek shock front due to thermal conduction can be found in the classical Spitzer conduction model. The width of the halo can be reduced to the simulation grid size in conductive flux-limited models. In both cases, NEI significantly affects ion population distributions and causes under-ionized features inside the reconnection current sheet as well as the thermal halo region.

2. In an ideal Petschek reconnection current sheet, the two-dimensional spatial distribution of ion charge states can be estimated by analyzing the 1D plasma evolution along the outflow direction once the shock angle is known, assuming that the current sheet is uniform. However, MHD-NEI simulations will be necessary to obtain accurate ionization calculations because of the temperature variation in the reconnection outflow direction (Ko et al. 2010).

3. A dense reconnection current sheet generally reduces the effects of NEI, especially for $\rho > \sim 10^{10}\,\mathrm{cm}^{-3}$. On the other hand, the effects of NEI also substantially depend on the temperature of the observational targets: the higher charge states (e.g., Fe XX–Fe XXV) depart more from the EI results compared with the lower charge states (e.g., Fe XIV–Fe XVIII). This occurs because equilibration timescales for the higher ionization ions are substantially longer than those of the low ionization ions (Smith & Hughes 2010). Our results indicate that the dominant ions in extremely high-temperature reconnection current sheets (e.g., 16 MK and above) should be obtained by solving time-dependent ionization equations, while the most abundant ions in a relatively cool current sheet (e.g., 8 MK) are barely affected by NEI.

4. Synthetic EUV narrow-band SDO/AIA images are compared between the EI and NEI predictions. Inside the reconnection current sheet, the assumption of EI underestimated AIA 94, 131, 171, and 335 Å, and overestimated AIA 193 Å in typical high-temperature plasma (∼16 MK). Around the thermal halo regions, the variation in all AIA count rates substantially depends on the width of the halo region. This

model suggests that the gap between the different AIA intensity gradients (such as AIA 94, 131, 171, and 211 Å) around the shock front could serve as a possible diagnostic of shocks and halos.

We estimated the departure of the assumption of NEI from the assumption of EI on the reconstructed temperatures using multiple SDO/AIA band images in typical hot reconnection current sheets ($\sim 10^7$ K) and extremely high-temperature environments ($\sim$16 MK). The under-ionized nature inside the reconnection current sheet causes a significant underestimation of the EM reconstructed temperature. Near the current sheet edge, the NEI reconstructed temperature can be lower by $\sim$60% compared to the actual temperature. The results show that the apparent width of the hot current sheet based on the emission reconstruction method may decrease by $\sim$8% and 31% in different density situations ($\sim 10^{10}$ and $\sim 2.5 \times 10^9$ cm^{-3}).

In a vertical reconnection current sheet configuration formed during solar flare eruptions, bidirectional reconnection outflows have been revealed in our models. The upward reconnection outflows are under-ionized, similar to the Petschek-type reconnection plasma. The downward reconnection outflows appear to have a slower speed due to the line-tied boundary condition and the formation of flare loops. The temperature and density at the lower tip of the reconnection current sheet quickly drop, which may cause over-ionized features, opposite to the classical Petschek-type reconnection flows. In tenuous plasma situations (e.g., $\sim 2.5 \times 10^9$ cm^{-3}), the corresponding synthetic EI intensity ratios of multiple bands (AIA 94/131 Å, AIA 171/131 Å), therefore, could be significantly overestimated by about one order of magnitude comparing the NEI predictions.

The authors thank Jing Ye for suggestions that helped us perform the MHD simulations, and thank the anonymous reviewers for valuable comments that improved the paper. This work was supported by NSF grants AGS-1723313 and AST 2108438 to the Smithsonian Astrophysical Observatory. This work was also supported by NASA grants 80NSSC21K2044, 80NSSC19K0853, 80NSSC18K1129, and 80NSSC20K1318. CHIANTI is a collaborative project involving the George Mason University, the University of Michigan (USA), and the University of Cambridge (UK). The computations in this paper were conducted on the Smithsonian High Performance Cluster, Smithsonian Institution (https://doi.org/10.25572/SIHPC).

Software: Athena (Stone et al. 2008), NEI solver (Shen et al. 2015), ChiantiPy (Dere 2013), Astropy (Astropy Collaboration et al. 2013), SunPy (Mumford et al. 2022).

Appendix A
1D Shock-tube Problem

The shock-tube problem has been commonly used in MHD simulation as a standard test. Here, we perform a 1D shock-tube simulation based on the classical Sod shock-tube configuration where two constant states have been separated by a discontinuity at the beginning. We apply the solar coronal temperature (10^6–10^7 K) in this test and set up the nondimensional plasma density and gas pressure as the following: $\rho_l = 1$, $p_l = 0.025$, and $\rho_r = 0.125$,

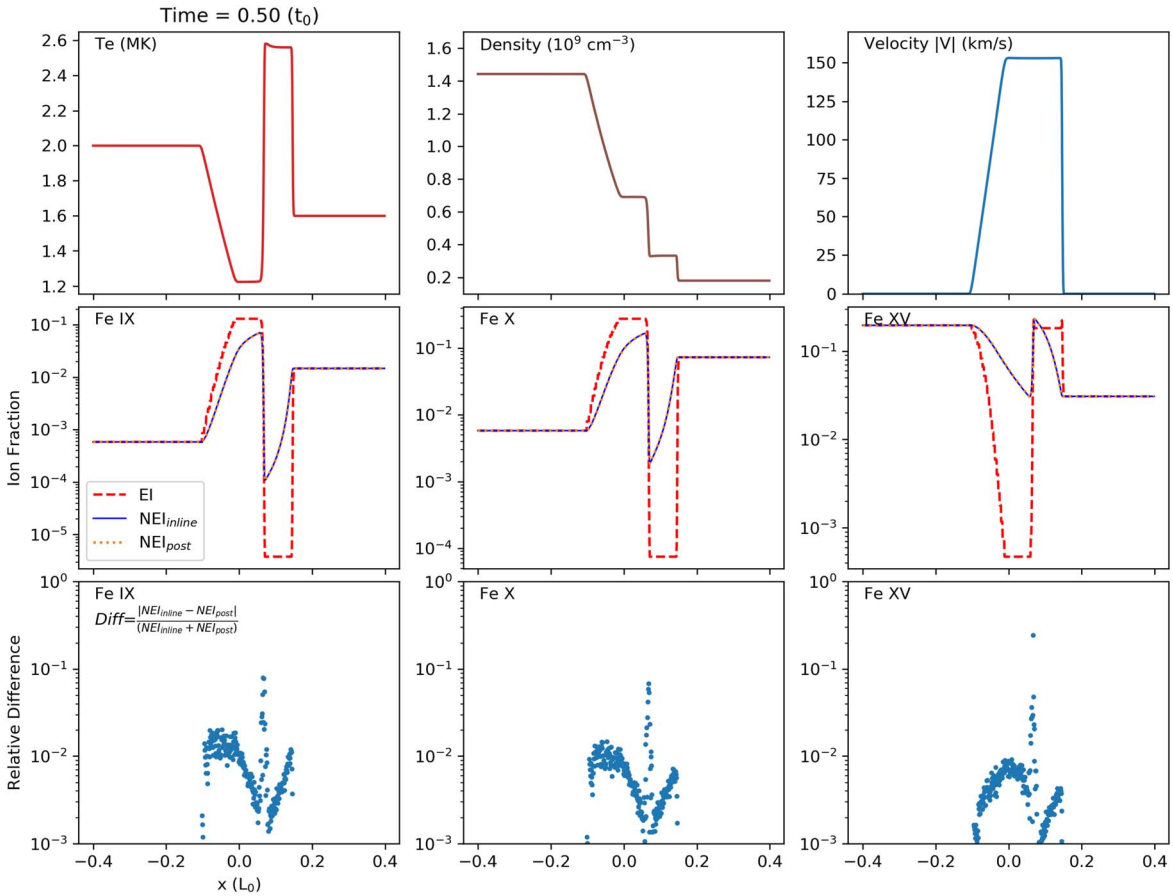

Figure 15. Comparison of the chosen ion fractions between the in-line NEI simulations and the post-processed NEI calculation at the sampling points in the 1D Sod shock test. The second row shows the ion fractions of Fe IX, Fe X, and Fe XIV, and the third row shows the relative difference between the in-line NEI and post-processed NEI fractions.

$p_r = 0.0025$. Here, the subscripts l and r indicate the left and right-hand sides of $x = 0$ along the x-axis, respectively. Figure 15 shows the results for the temperature, density, velocity, and several Fe ion fractions at $t = 0.5t_0$) on the grid of 1000 cells in the domain $-0.5 < x < 0.5$. In the second row of Figure 15, the Fe IX, Fe X, and Fe XV ion fraction distributions as functions of x are plotted. The red-dashed lines represent the EI profiles, which strongly depend on plasma temperature, while the blue lines represent the in-line NEI results. For comparison, we also perform the post-processed NEI calculation (see the red-dotted lines) by tracing the trajectory of plasma movements and solving the time-dependent ionization equation in the Lagrangian framework to obtain the ion fractions (e.g., Shen et al. 2013a, 2015). In the third row, we checked the difference between the in-line NEI results and post-processed NEI calculations by plotting diff $= \frac{\mathrm{NEI_{inline}} - \mathrm{NEI_{post}}}{\mathrm{NEI_{inline}} + \mathrm{NEI_{post}}}$. It is clear that the errors are lower than about 2% for the above-chosen ions in the post-shock regions. Diff could be larger at a few points around the shocks caused by the interpolation process (both spatially and temporally) while tracing the movement of the plasma in the post-processed NEI calculations. Therefore, we expect the error could be minor with fine simulation cells and outputting intervals.

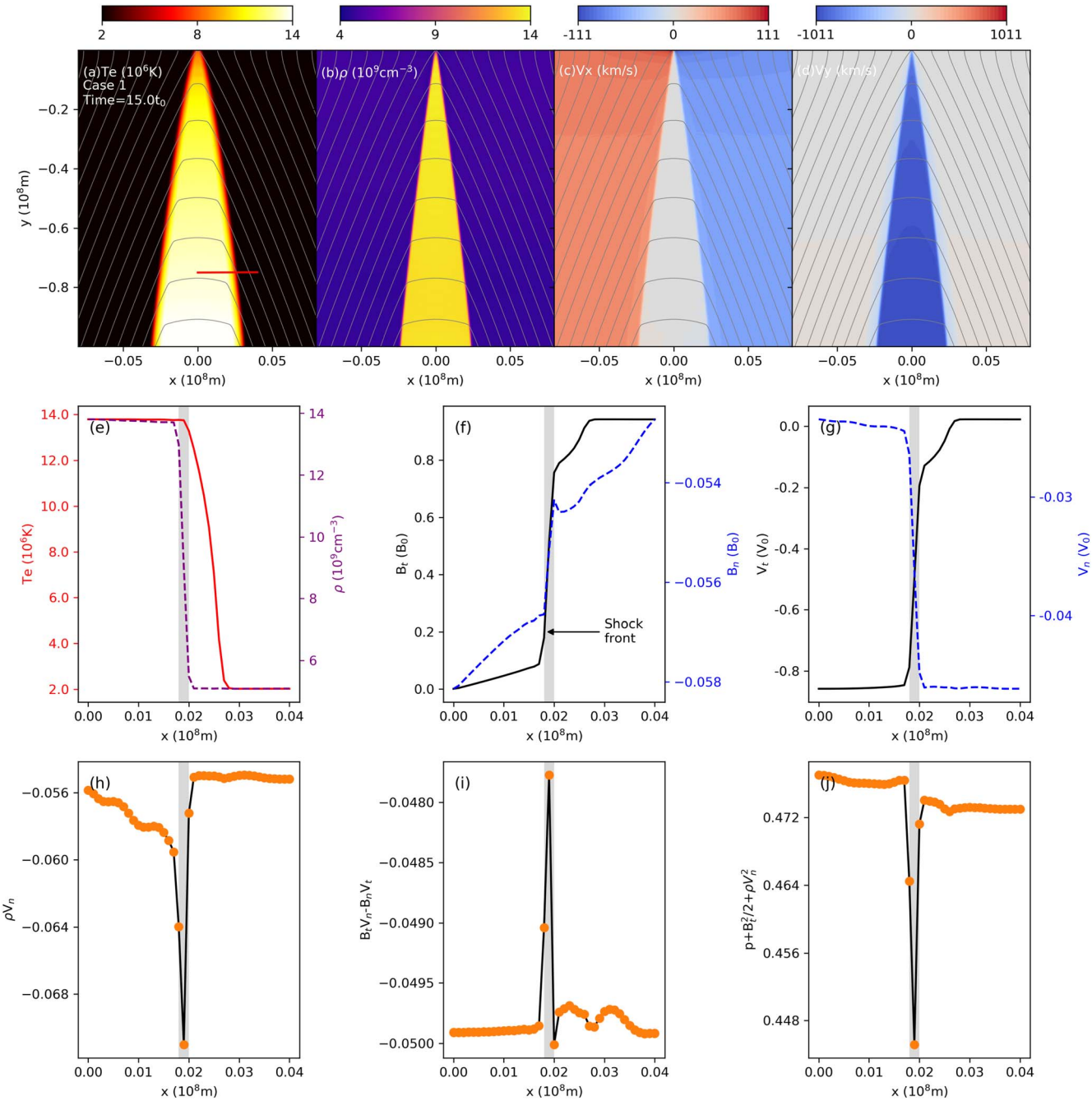

Figure 16. The slow-mode shocks in a Petschek-type reconnection simulation with the classical Spitzer thermal conduction coefficients. (a)–(d) The temperature, density, and plasma velocity around the reconnection X-point, and a pair of slow-mode shocks. The solid gray contours represent the magnetic field lines. (e)–(g) Distribution of the primary variables crossing the shock front along the red sampling line shown in panel (a). The vertical gray shadows indicate the position of the shock front. Here, B_t (and V_t) is the transverse component of the magnetic field (and velocity), and B_n (and V_n) is the normal component of the shock front, respectively. (h)–(j) Nondimensional mass flux, magnetic flux, and energy flux distribution that continues crossing the slow-mode shocks.

Appendix B
Jump Condition

In order to confirm the shock properties in detail, we check the primary variables across the shock front along the red solid line in Figure 16(a)). This sampling line is chosen to be perpendicular to the shock surface, and has an angle of $1^{\circ}.35$ to the x-direction. Figures 16(e)–(g) show that these variables jump from the shock upstream (right side along the x-direction) to the downstream (left side), including temperature, density, magnetic, and velocity field. The shock front is indicated by the vertical gray shadows. It is interesting that a *thermal halo* region, outside the high-density reconnection current sheet (see Figure 16(a), (e)), can also be clearly seen due to the thermal conduction with the classical Spitzer thermal conduction coefficient in this simulation. However, this thermal halo could be overestimated in the model, and has been discussed in the above sections. As shown in the third row of Figure 16, we further calculated the mass flux component, magnetic flux component, and momentum flux along the cut line. As can be seen in Figures 16(h) and (i), the relative changes in ρV_n and $B_t V_n - B_n V_t$ are roughly 6% and less than ∼2% between the upstream and downstream of the shocks, respectively. The momentum flux component is also conserved, and the relative changes between upstream and downstream are still less than ∼1% as shown in panel (j). It is noticed that there are unavoidable measurement errors when estimating the direction of the shock front, which may cause slight deviations in both the interpolated transverse and normal components of the primary variables. However, the conservation conditions of primary variables are basically satisfied with the Rankine–Hugoniot relation between the upstream and downstream.

Appendix C
EUV Emission

Figure 17 shows the temperature response function for six SDO/AIA channels. The response function with 14 of the most abundant elements can be a good approximation in most coronal temperature ranges.

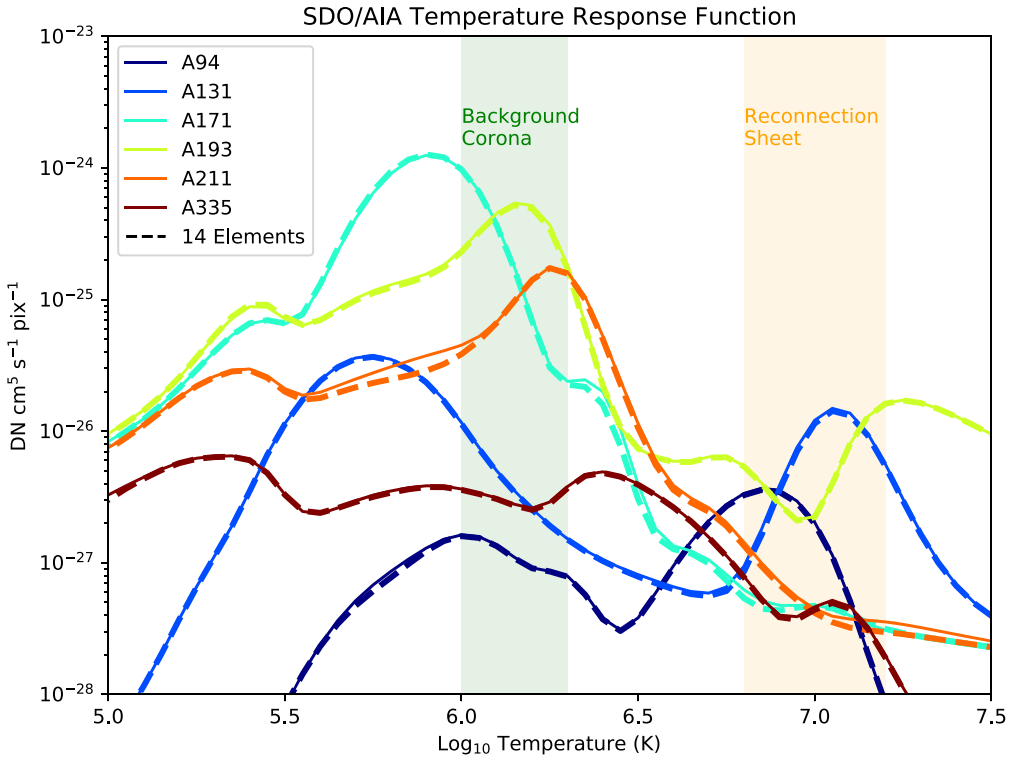

Figure 17. Temperature response function for six SDO/AIA channels. The solid lines are calculated using the CHIANTI database (Dere et al. 2019), assuming EI and the coronal abundance (Feldman 1992). The dotted lines denote the most abundant 14 elements (H, He, C, N, O, Ne, Mg, Al, Si, S, Ar, Ca, Fe, and Ni) calculated in this work. The green and orange shaded regions indicate the temperature ranges of the background corona and reconnection current sheets, respectively.

ORCID iDs

Chengcai Shen https://orcid.org/0000-0002-9258-4490
John C. Raymond https://orcid.org/0000-0002-7868-1622
Nicholas A. Murphy https://orcid.org/0000-0001-6628-8033

References

Astropy Collaboration, Robitaille, T. P., Tollerud, E. J., et al. 2013, A&A, 558, A33
Bhattacharjee, A., Huang, Y.-M., Yang, H., & Rogers, B. 2009, PhPl, 16, 112102
Carmichael, H. 1964, NASSP, 50, 451
Chen, P. F., Fang, C., Tang, Y. H., & Ding, M. D. 1999, ApJ, 513, 516
Cheng, X., Li, Y., Wan, L. F., et al. 2018, ApJ, 866, 64
Cheung, M. C. M., Boerner, P., Schrijver, C. J., et al. 2015, ApJ, 807, 143
Ciaravella, A., & Raymond, J. C. 2008, ApJ, 686, 1372
Ciaravella, A., Raymond, J. C., Li, J., et al. 2002, ApJ, 575, 1116
Cowie, L. L., & McKee, C. F. 1977, ApJ, 211, 135
Dere, K. 2013, ChiantiPy: Python Package for the CHIANTI Atomic Database, Astrophysics Source Code Library, ascl:1308.017
Dere, K. P., Del Zanna, G., Young, P. R., Landi, E., & Sutherland, R. S. 2019, ApJS, 241, 22
Feldman, U. 1992, PhyS, 46, 202
Forbes, T. G. 1986, ApJ, 305, 553
Forbes, T. G., & Priest, E. R. 1987, RvGeo, 25, 1583
Forbes, T. G., Seaton, D. B., & Reeves, K. K. 2018, ApJ, 858, 70
Foster, A., Smith, R., Brickhouse, N. S., et al. 2018, AAS Meeting, 231, 253.03
Fryxell, B., Olson, K., Ricker, P., et al. 2000, ApJS, 131, 273
Hirayama, T. 1974, SoPh, 34, 323
Huang, Y.-M., & Bhattacharjee, A. 2016, ApJ, 818, 20
Hughes, J. P., & Helfand, D. J. 1985, ApJ, 291, 544
Imada, S. 2021, ApJL, 914, L28
Imada, S., Murakami, I., Watanabe, T., Hara, H., & Shimizu, T. 2011, ApJ, 742, 70
Ko, Y.-K., Raymond, J. C., Lin, J., et al. 2003, ApJ, 594, 1068
Ko, Y.-K., Raymond, J. C., Vršnak, B., & Vujić, E. 2010, ApJ, 722, 625
Kopp, R. A., & Pneuman, G. W. 1976, SoPh, 50, 85
Landi, E., Alexander, R. L., Gruesbeck, J. R., et al. 2012, ApJ, 744, 100
Landi, E., & Lepri, S. T. 2015, ApJL, 812, L28
Lazarian, A., & Vishniac, E. T. 1999, ApJ, 517, 700
Lee, J.-Y., Raymond, J. C., Reeves, K. K., et al. 2019, ApJ, 879, 111
Lin, S.-C., Liu, Y.-H., & Li, X. 2021, PhPl, 28, 072109
Lionello, R., Downs, C., Linker, J. A., et al. 2019, SoPh, 294, 13
Loureiro, N. F., Schekochihin, A. A., & Cowley, S. C. 2007, PhPl, 14, 100703
Masai, K. 1984, Ap&SS, 98, 367
Mei, Z., Shen, C., Wu, N., et al. 2012, MNRAS, 425, 2824
Mumford, S. J., Freij, N., Christe, S., et al. 2022, SunPy, v3.1.5, Zenodo, doi:10.5281/zenodo.591887
Ni, L., Germaschewski, K., Huang, Y.-M., et al. 2010, PhPl, 17, 052109
O'Dwyer, B., Del Zanna, G., Mason, H. E., Weber, M. A., & Tripathi, D. 2010, A&A, 521, A21
Orlando, S., Peres, G., Reale, F., Rosner, R., & Siegel, A. 2003, MmSAI, 74, 643
Parker, E. N. 1957, JGR, 62, 509
Petschek, H. E. 1964, NASSP, 50, 425
Reeves, K. K., & Golub, L. 2011, ApJL, 727, L52
Reeves, K. K., Linker, J. A., Mikić, Z., & Forbes, T. G. 2010, ApJ, 721, 1547
Reeves, K. K., Török, T., Mikić, Z., Linker, J., & Murphy, N. A. 2019, ApJ, 887, 103
Rosner, R., Low, B. C., & Holzer, T. E. 1986, Physics of the Sun, Vol. 2 (Dordrecht: Reidel), 135
Savage, S. L., McKenzie, D. E., Reeves, K. K., Forbes, T. G., & Longcope, D. W. 2010, ApJ, 722, 329
Schmelz, J. T., Reames, D. V., von Steiger, R., & Basu, S. 2012, ApJ, 755, 33
Seaton, D. B., Bartz, A. E., & Darnel, J. M. 2017, ApJ, 835, 139
Seaton, D. B., & Forbes, T. G. 2009, ApJ, 701, 348
Shen, C., Kong, X., Guo, F., Raymond, J. C., & Chen, B. 2018, ApJ, 869, 116
Shen, C., Lin, J., & Murphy, N. A. 2011, ApJ, 737, 14
Shen, C., Lin, J., Murphy, N. A., & Raymond, J. C. 2013a, PhPl, 20, 072114
Shen, C., Raymond, J. C., Mikić, Z., et al. 2017, ApJ, 850, 26
Shen, C., Raymond, J. C., & Murphy, N. A. 2015, Non-equilibrium Ionization Code, Zenodo, doi:10.5281/zenodo.272609
Shen, C., Raymond, J. C., Murphy, N. A., & Lin, J. 2015, A&C, 12, 1
Shen, C., Reeves, K. K., Raymond, J. C., et al. 2013b, ApJ, 773, 110
Shibata, K., & Magara, T. 2011, LRSP, 8, 6
Smith, R. K., & Hughes, J. P. 2010, ApJ, 718, 583
Stone, J. M., Gardiner, T. A., Teuben, P., Hawley, J. F., & Simon, J. B. 2008, ApJS, 178, 137
Sturrock, P. A. 1968, in IAU Symp. 35, Structure and Development of Solar Active Regions, ed. K. O. Kiepenheuer, 471
Sweet, P. A. 1958, in IAU Symp. 6, Electromagnetic Phenomena in Cosmical Physics, ed. B. Lehnert (Cambridge: Cambridge Univ. Press), 123
Szenicer, A., Fouhey, D. F., Munoz-Jaramillo, A., et al. 2019, SciA, 5, eaaw6548
Warren, H. P., Brooks, D. H., Ugarte-Urra, I., et al. 2018, ApJ, 854, 122
Winter, H. D., Martens, P., & Reeves, K. K. 2011, ApJ, 735, 103
Yokoyama, T., & Shibata, K. 1997, ApJL, 474, L61
Yokoyama, T., & Shibata, K. 2001, ApJ, 549, 1160
Zhang, G.-Y., Foster, A., & Smith, R. 2018, ApJ, 864, 79
Zhang, G.-Y., Slavin, J. D., Foster, A., et al. 2019, ApJ, 875, 81